Department of Physics and Astronomy
University of Heidelberg

Bachelor Thesis in Physics
submitted by

Lukas Layer

born in Schwäbisch Hall (Germany)

2015

Development of a fast simulation tool for vertexing studies in ALICE

This Bachelor Thesis has been carried out by Lukas Layer at the
Physikalisches Institut at the University of Heidelberg
under the supervision of
Dr. Silvia Masciocchi

Abstract

The measurement of open heavy flavour hadrons plays a key role in the physics program of the ALICE experiment. For the heavy flavour analysis it is crucial to determine primary and secondary vertices with high precision. For this a new version of the KFParticle vertexing package, that provides powerful tools for these challenges, is tested. In order to verify the algorithmic implementation of the code, a Unit Test has been developed. To have full control over the input of the test, a fast simulation tool is implemented. Different observables of the decay $D^0 \to \pi^+ K^-$ and their charge conjugates are studied. The results are compared to other vertexing packages. To verify the fast simulation the same tests were repeated on full simulation and the results compared. The recalculation of the primary vertex with different functionalities is investigated.

Zusammenfassung

Die Messung von Hadronen, die Charm und Beauty Quarks enthalten, spielt eine wichtige Rolle im Programm des ALICE Experiments. Für die Analyse dieser Messungen ist es entscheidend primäre und sekundäre Vertizes mit hoher Präzission zu messen. Hierfür wird eine neue Version des KFParticle Vertexing Paketes getestet, das mächtige Funktionen für diese Aufgaben bereitstellt. Um die Implementation des Algorithmus zu verifizieren, wurde ein Unit Test entwickelt und eine Fast Simulation implementiert, die es ermöglicht Kontrolle über den Input zu erhalten. Verschiedene Observable des Zerfalls $D^0 \to \pi^+ K^-$ werden untersucht und mit anderen Vertexing Paketen verglichen. Um die Fast Simulation zu verifizieren werden die selben Tests in einer vollen Simulation durchgeführt und die Resultate verglichen. Die Berechnung des primären Vertex wird mit verschiedenen Funktionen untersucht.

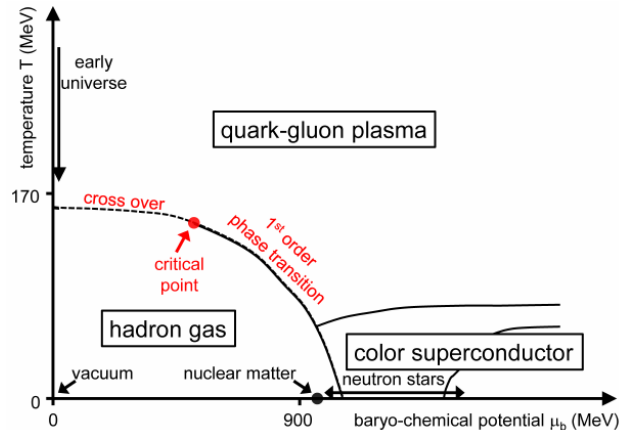# Contents

1 The Quark Gluon Plasma

Figure 1: Phase diagramm of QCD [1]

Quantum ChromoDynamics (QCD) is the theory describing the strong interaction between quarks [2] which are the building blocks of matter and gluons which are the carriers of the strong force. One of the crucial tests of QCD is the quantification of the behaviour of strongly interacting matter in the high temperature and high density limit. Under these conditions, QCD predicts the existence of a deconfined medium that is called the Quark Gluon Plasma (QGP). Deconfinement means that the colourless hadrons turn into a plasma consisting of asymptotically free coloured quarks and gluons. Since observations have shown that no free quarks exist at the temperature and densities that we live in, a phase transition has to occur. The phase diagram of QCD is shown in figure 1.

The mass of bound states of hadrons is not only determined by valence quarks, but also by virtual seaquarks and gluons. This leads to the fact that the constituent quark mass $M_{u,d} \sim 300$MeV of up and down quarks is significantly higher than the calculated bare mass m_q that is in the order of a few MeV. Since the QCD Lagrangian contains a symmetry, called chiral symmetry, for zero bare quark mass, the constituent quark mass $M_{u,d} > 0$ implies a breaking of this symmetry. The chiral symmetry of the QCD Lagrangian is predicted to be restored again, because the constituent quark mass becomes zero.

The transition from the hadronic to the deconfined state is supposed to occur at a critical temperature T_C [3]. Using a naive calculation for an ideal gas of massless pions and an ideal quark gluon plasma with two flavours and three colours, the critical temperature can be approximated by assuming that the gases are following the Stefan-Boltzmann law: $P \sim T^4$ (fig. 2). Since thermodynamics predicts that a system always chooses the state of lowest free energy and thus highest pressure, a rough estimate of T_C can be found by a simple extrapolation as $T_C \approx 150$MeV. The same simple estimation can be made for the energy density: in this model the phase transition is of first order and thus an increase of the energy density due to latent heat of the deconfinement is obtained. To get more precise results advanced theoretical concepts have been developed. Since the standard way of solving QCD problems with perturbative calculations (pQCD) is not applicable in this region, a large number of theoretical approaches [4] have been developed. To calculate the critical temperature, lattice QCD is used. The critical temperature is depending on the baryo-
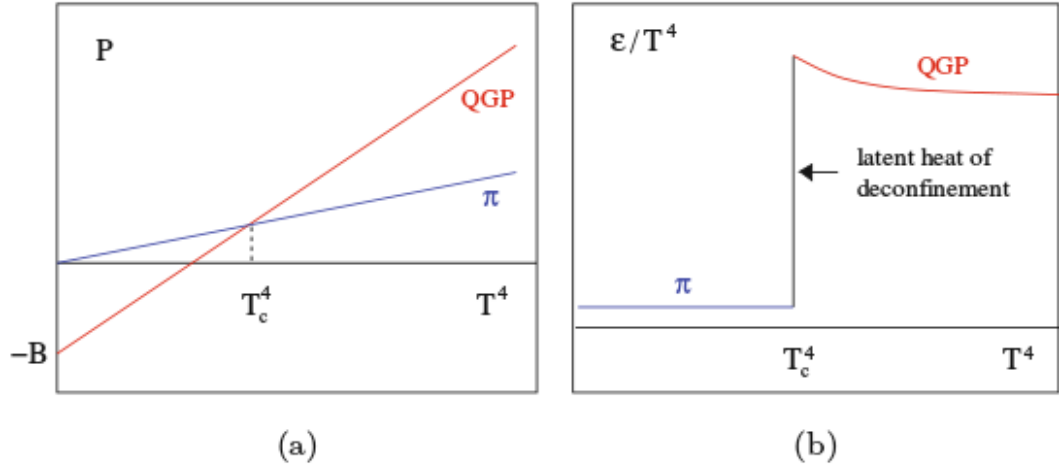
Figure 2: The left panel shows a simple extrapolation of the critical temperature T_C using an ideal gas of pions and quarks. B is the bag pressure, which takes into account differences between the vacuum and ground state for partons in the QGP. The right panel shows the energy density in the two phase ideal gas model [3].

chemical potential which is the energy needed to add a baryon to the the thermodynamic system. For high energy collisions at the Large Hadron Collider (LHC), the baryo-chemical potential is vanishing and the theoretical calculations predict a critical temperature in the range of 150MeV$< T_C <$ 180MeV. Furthermore, lattice QCD states that beyond a critical point, the phase transition is not of first order any more, but of the crossover type. Both, the critical temperature and the nature of the phase transition are under investigation. The high energy density in heavy-ion collisions gives the possibility to study the behaviour of hot and dense matter in a unique way. Results from former heavy ion experiments imply several properties of the QGP state [1]. The time-scale for the partons of the produced fireball to reach equilibrium is of the order of 1fm/c for the collision energies at the LHC. The fireball evolves after thermalization following the laws of relativistic hydrodynamics. It expands, cools down and undergoes hadronization, which means that new hadrons are formed at the phase boundary. If the collision is not fully central, the initial spatial asymmetry reflects in the distribution of the momenta of the hadrons. The centrality is a parameter that is related to the absolute value of the impact parameter vector that connects the centres of the two colliding nuclei. In momentum space the anisotropy is quantified by a Fourier expansion, where the second harmonic coefficient, called elliptic flow, is supposed to be sensitive to the early dynamics of the collision. Measurements of the elliptic flow imply that the QGP evolves close to a perfect fluid. Due to the high density of the fluid, jets from the hard scattering of partons are expected to lose energy in the medium. Furthermore, in heavy-ion collider experiments at lower energies a suppression of the quarkonium state J/ψ was observed that was associated with colour charge screening. However, going to higher collision energies an enhancement of J/ψ is predicted [5], due to the statistical recombination of the quarks at the phase boundary or by coalescence of charm quarks in the medium. A key role in the challenge of quantifying the QGP is played by the measurement of open heavy flavour hadrons which is discussed in the following sections.

2 The ALICE Experiment

ALICE is an acronym for A Large Ion Collider Experiment and is one of the four main experiments at the Large Hadron Collider (LHC) at CERN, Geneva. ALICE is optimized for the extreme charged particle multiplicities arising from the collision of heavy nuclei and thus provides excellent conditions to study the behaviour of matter under extreme temperatures and densities. Besides measurements in lead-lead collisions, ALICE measures the collisions of proton-proton and lead-proton in order to have reference measurements to distinguish effects caused by the QGP from effects caused by other sources. In the following an overview of the detector and the event reconstruction will be given with special emphasis on the issues related to the reconstruction of the charged particle tracks. This section is inspired by material in the ALICE performance reports [6] [7] [8].

2.1 The Detector
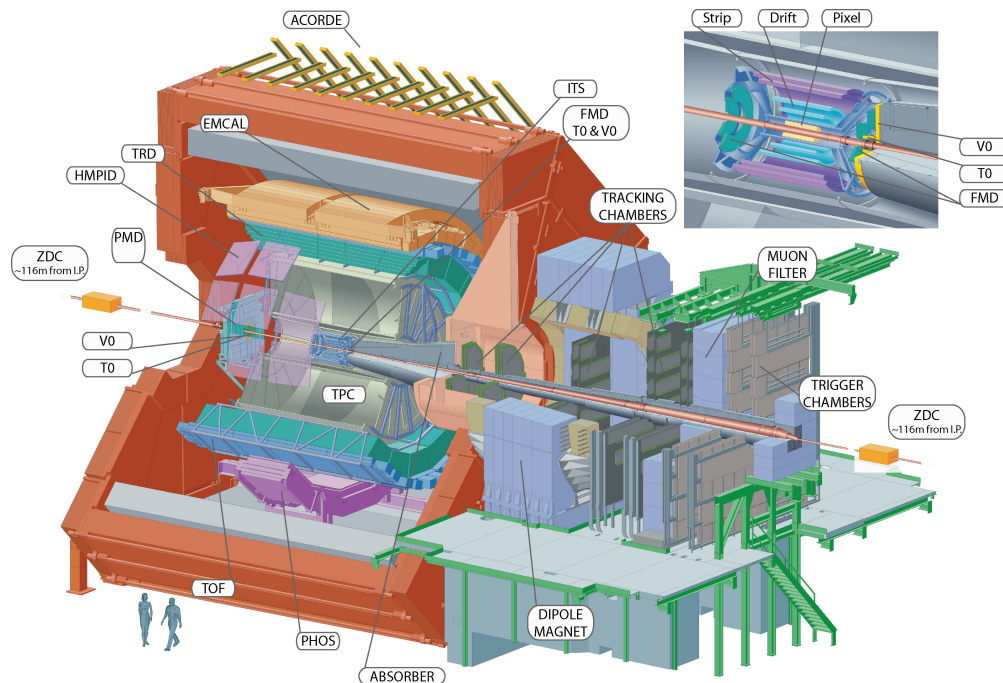
Figure 3: Overview over the ALICE detector [6]

The ALICE detector is presented in figure 3. Beginning from the inside, the detector consists out of the following elements. The central barrel detectors: the Inner Tracking System (ITS) used for the high precision determination of vertices and tracking, the Time Projection Chamber (TPC) that serves as the main tracking element and provides particle identification (PID) via dE/dX measurements, the Transition Radiation Detector (TRD) used for the tracking and the identification of charged particles via transition radiation and dE/dX, the Time-Of-Flight (TOF) that provides PID via the measurement of the particle velocity at intermediate momenta, the Electromagnetic Calorimeter (EMCal), the Photon Calorimeter (PHOS) and the High Momentum Particle Identification Detector (HMPID). ITS, TPC and TOF cover the entire azimuthal range, and a pseudo rapidity range of about $-0.9 < \eta < 0.9$

and are divided in 18 segments in azimuth. Sectors in azimuth for TRD, PHOS and EMCal have been added over the years. The central barrel detectors are surrounded by a solenoid magnet that provides a magnetic field of 0.5T.

In the forward rapidity region the Photon Multiplicity Detector (PMD) and the Forward Multiplicity Detector (FMD) provide measurements of photons and charged particles. The T0 detector measures the time and the longitudinal position of the interaction, while the V0 detector measures charged particles and is used for triggering and the measurement of centrality and the angle of the event plane in Pb-Pb. To resolve the ambiguity between the most central and the most peripheral collisions, that both have few spectator nucleons, an electromagnetic calorimeter (ZEM) is used. The Zero Degree Calorimeter (ZDC) is used for measurements of the centrality. Light vector mesons and J/ψ are measured by the MUON spectrometer in forward rapidity, as well as high-p_T muons originating from charm and beauty decays.

2.2 The Inner Tracking System

The Inner Tracking System consists of six layers of silicon detectors. The ITS is designed to provide the determination of the primary vertex and displaced secondary vertices coming from Heavy Flavour decays with a precision in the order of a few tens of microns. The spatial resolution is presented in table 1 . Moreover, the ITS provides PID for low momenta tracks and improves the momentum resolution copared to the TPC stand-alone tracking. It is also possible to reconstruct tracks at very low momenta or high momenta, that traverse the TPC in blind regions by a standalone tracking algorithm. Due to the high particle density in the first two layers, Silicon Pixel Detectors (SPD) have been chosen for the first two layers and Silicon Drift Detectors (SDD) for the following two layers. The high resolution of these silicon detectors also provide a precise measurement of the impact parameter. The outer two layers, where the hit density is lower, are equipped with Silicon Strip Detectors (SSD). The first two layers have an extended η range. Since the resolution of the momentum and the impact parameter is dominated by multiple scattering effects for low momenta, the material budget of the silicon detectors are kept to the minimum. The ITS is crucial for the global track fit and the track quality depends heavily on the hits in the ITS.

Table 1: Resolution of the main tracking devices [8]

Detector	Radius R (cm)	η range	Resolution $R\phi$ (μm)	Resolution z (μm)
SPD	3.9 & 7.6	1.98	12	100
SDD	15.0 & 23.9	0.9	38	28
SSD	37.8 & 42.8	0.9	20	830
TPC	84.5 - 246.6	0.9	1100 - 800	1250 - 1100

2.3 The Time Projection Chamber

The TPC is the main tracking detector in ALICE. It provides robust and efficient tracking in a large momentum range, as well as a high momentum resolution and is optimized for

very high particle densities. Quantitative values for the track resolution and the momentum resolution will be investigated in chapter 6. By measuring the energy loss in the drift gas, the TPC provides particle identification for charged particles. The TPC is divided into two volumes, separated by an electrode that generates the drift field. The cylindrical field cage of the TPC is filled with a gas mixture. The primary electrons caused by the traversing of a charged particle drift to the end plates on either side. Here multi-wire proportional chambers with cathode pad readout divided in 18 trapezoidal sectors are installed. At the readout plates a radial coordinate R and an azimuthal coordinate ϕ is measured. The third coordinate in z direction is calculated from the drift time of the electrons. The maximal numbers of cluster that can be measured in the TPC is 159. An important issue for the TPC is the alignment with the other tracking detectors in order to perform the global track fit supported by the other subdetectors. The blind regions between the chambers have significant influence on the spatial resolution and the momentum resolution of tracks traversing these sectors.

2.4 Event reconstruction

The first step towards the reconstruction of the tracks is the conversion of their detector response into clusters and the calculation of their position and their errors. The calculated position of the cluster is interpreted as the crossing point of the track. After this the preliminary position of the primary vertex is determined using the first two layers of the ITS. The preliminary primary vertex is the point where most of the tracklets, defined as lines through one cluster in the first and the second SPD, converge.

The next step is the track finding. Track seeds are built at large radii in the TPC using two adjacent clusters and the preliminary vertex as a constraint. Besides three clusters without the vertex constraint are used to find tracks not originating from the primary vertex. The seeds are propagated towards the primary vertex and clusters are assigned within certain proximity cuts using the Kalman Filter algorithm. Only tracks that contain at least 20 clusters and miss not more than 50 % of the expected clusters depending on the track position are kept. At the same time, a preliminary PID is obtained by a dE/dx measurement.

In the next step, the tracks are propagated to the ITS and become the seeds for the track finding in the ITS. Since the track density is too high in the ITS, decision trees within certain cuts are built and the tracks are sorted according to their χ^2. Algorithms to avoid the sharing of clusters between tracks are applied. In the end the tracks with the highest quality according to their χ^2 are kept. The clusters not used in the ITS-TPC track fit are used for the ITS standalone tracking.

The found tracks are propagated outward using the Kalman Filter and various information are updated at each step. The tracks are matched to tracklets of the TRD, TOF clusters and signals in EMCal, PHOS and HMPID. The final step of the track reconstruction is the refit of the tracks inward starting at the outer radius of the TPC using again the Kalman Filter algorithm. The parameters of the track state vector and its covariance matrix are calculated.

The tracks are extrapolated to the distance of closest approach (DCA) to the nominal primary vertex and the final primary vertex position is determined by a fit that weights the used tracks which helps to suppress outliers. To achieve a higher transverse resolution in low-multiplicity events, the so called diamond constraint is applied as an independent mea-

surement depending on the transverse size of the luminous region. The size of the luminous region can be obtained after a few ten thousand events.

Secondary vertices (V^0) from photon conversions and from the decay of K_s^0, Λ^0, Ξ^- and Ω^-
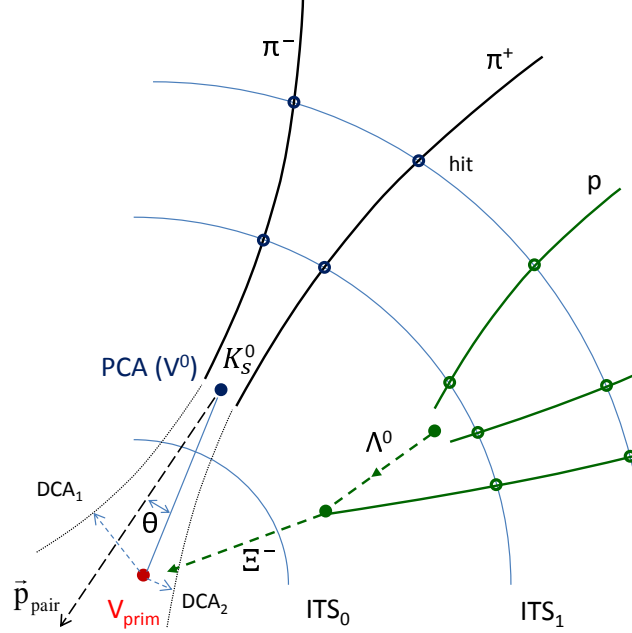
Figure 4: Topology of V^0 decays. Solid lines are reconstructed tracks. Tracks extrapolated to the primary vertex are represented with dashed lines. The pointing angle is denoted with θ. The figure is not in a realistic scale. [6].

and their charge conjugates are calculated from unlike sign tracks exceeding a certain DCA to the primary. Cuts on the DCA between the tracks and the pointing angle to the primary vertex are applied. The pointing angle is the angle between the total momentum vector of both daughter tracks and the line connecting the secondary with the primary vertex. The topology of a V^0 decay is shown in figure 4. The same algorithm can not be used to find secondary vertices from heavy flavour decays. However, the ALICE offline reconstruction framework AliROOT provides tools to calculate more complicated secondary vertices, which are important for the heavy flavour (HF) program described in the next section.

3 Open Heavy Flavour Hadrons

3.1 Overview

Because of their large masses [1], charmed quark pairs ($m_c = 1.29^{+0.05}_{-0.11} GeV$) and beauty quark pairs ($m_b = 4.19^{+0.18}_{-0.06} GeV$) are only produced in hard partonic scattering. This takes place in the initial phase of the collision. Therefore heavy quarks are produced before the formation of the QGP and thus experience the full evolution of the QGP. One production mechanism for heavy quarks is, amongst various others, gluon-gluon fusion. Because of their motion in the QGP medium heavy quarks contain information about the collision history and therefore their measurement in the final state can be used to characterize the QGP. With the high beam energies of the LHC, ALICE provides significantly larger cross sections compared to previous heavy-ion experiments of other colliders. The measurement of heavy flavour in pp collisions serves as a test for perturbative QCD calculations and provides a benchmark for the measurements in heavy ion collisions.

Considering heavy flavour production in nucleus-nucleus collisions without nuclear effects, the heavy flavour yields are expected to scale with the number of binary collisions. Since measurements in the past at lower energies indicated that there are deviations from this scaling, heavy flavours are used to quantify nuclear modifications. One distinguishes between two types of modifications: initial state effects, which are mainly due to the fact that the parton distributions in nuclei are different from the distributions in nucleons and final state effects. The final state effects are caused by interactions with the QGP and are the aim of the investigations of the ALICE HF program.

The final state effects are supposed to change the distribution of heavy flavour respectively their decay products in the phase space. Since the energy loss of heavy flavour in matter is expected to depend on the energy density of the matter, the p_T distributions of HF hadrons and their decay products are expected to be softened in nucleus-nucleus collisions compared to the distributions in pp. There are two main processes of energy loss for quarks. First there is radiative energy loss because of gluon radiation caused by the QGP. QCD states that this is not the same for quarks and gluons. Together with the so called dead-cone effect, which states that gluon radiation is suppressed at small angles, while the angle depends on the quark mass, radiative energy loss leads to a mass hierarchy of high p_T hadron suppression [1]. The suppression of hadrons is quantified by the nuclear modification factor R_{AA}

$$R_{AA} = \frac{dN_{AA}/p_T}{dN_{pp}/p_T} \frac{1}{<N_{coll}>} \tag{1}$$

where $< N_{coll} >$ is the number of binary collisions and dN_{AA}/p_T and dN_{pp}/p_T are the differential invariant yields of nucleus-nucleus and pp collisions respectively. The expected hierarchy in hadron suppression is:

$$R^{\pi}_{AA} < R^c_{AA} < R^b_{AA} \tag{2}$$

The second important mechanism that causes energy loss in the QGP is the collisional energy loss. This originates from the elastic scattering of the quarks and is more important for heavy quarks than for light quarks [1].
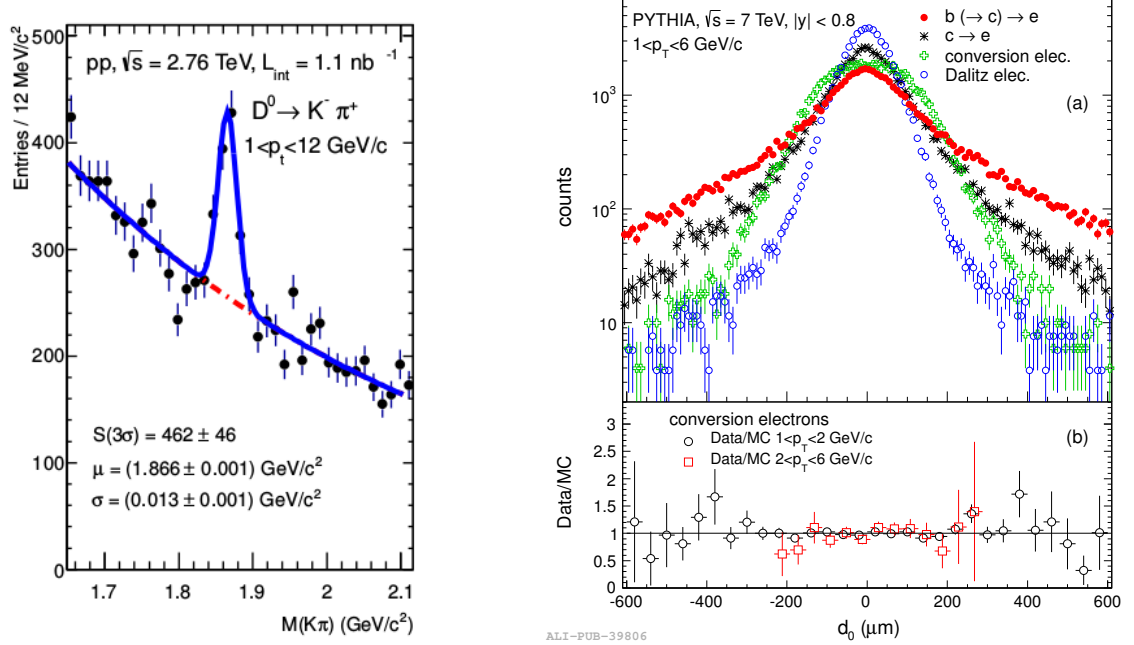
(a) Example for an invariant mass analysis for the decay of a D^0 in a pion and a kaon [9]

(b) a) Simulation of the impact parameter of different electron sources b) Ratio of the simulated conversion electrons to the measured conversion electrons [10]

Figure 5

3.2 Measurement techniques in ALICE

Due to the short lifetime of heavy flavour hadrons, a precise measurement is difficult. In table 2 the mass and the $c\tau$ of some heavy flavour hadrons is shown. A possible strategy [9] to measure D^0 and D^+ is the direct reconstruction by their decay products via the reconstruction and selection of the secondary vertex topologies that are significantly displaced with respect to the primary vertex. This is possible because of the high resolution of the ITS. Together with TPC and TOF PID of the kaon, this allows a reduction of the background. The signal is then extracted from an invariant mass analysis (5a). Important topological cuts made for the selection are, among others, applied to the DCA between the daughters, the impact parameter of the daughters, the displacement of the secondary vertex and the pointing angle of the reconstructed meson. The obtained raw yields are further corrected for geometrical acceptances and efficiencies of reconstruction and identification. Moreover feeddown corrections obtained from theory are applied. A feeddown is a D meson coming from the decay of a B meson, while a prompt D meson is coming directly from the primary vertex. From the corrected yields, the differential cross section can be calculated which is a crucial test for predictions of pQCD. The same method can not be used for beauty decays, because of their small number of decay channels with a limited number of daughters. A full hadronic reconstruction requires that all daughters are in the acceptance of the detector which is not the case for many decay channels of beauty hadrons.

A second method [11], giving access to the measurement of HF electrons originating from

Table 2: Mass and $c\tau$ of heavy flavour hadrons [1].

Observable	$D^{+/-}$	D^0	$B^{+/-}$	B^0
$c\tau$ (μm)	312 ± 2	123 ± 1	492 ± 2	455 ± 2
Mass (GeV)	1.8696 ± 0.0002	1.8648 ± 0.0002	5.2792 ± 0.0003	5.2795 ± 0.0003

beauty hadron decays, is the separation of electrons via their impact parameter. This method allows the statistical separation of beauty and charm mesons which is important to quantify the mass dependence of the energy loss as described in the previous section. Electrons are identified using the PID of TPC and TOF. The background is dominated by Dalitz decays of light mesons and photon conversions. However, subtracting this background from the total number of electrons in order to obtain beauty contributions leads to large uncertainties, because both samples are in the same order of magnitude. This uncertainty can be reduced by exploiting the fact, that the width of the impact parameter distributions is different for beauty, charm, Dalitz and conversion electrons as presented in figure 5b. By making a p_T dependent cut on the impact parameter, the signal to background ratio for beauty electrons improves. Thus the uncertainties after the subtraction of the background electrons decrease significantly. A second method is to compare the impact parameter distribution of the electron sources of MC templates to the distribution of the impact parameter of all measured electrons. By fitting the templates, the individual contribution of the real data can be estimated.

Further measurement strategies are reviewed in [1].

3.3 Recent results

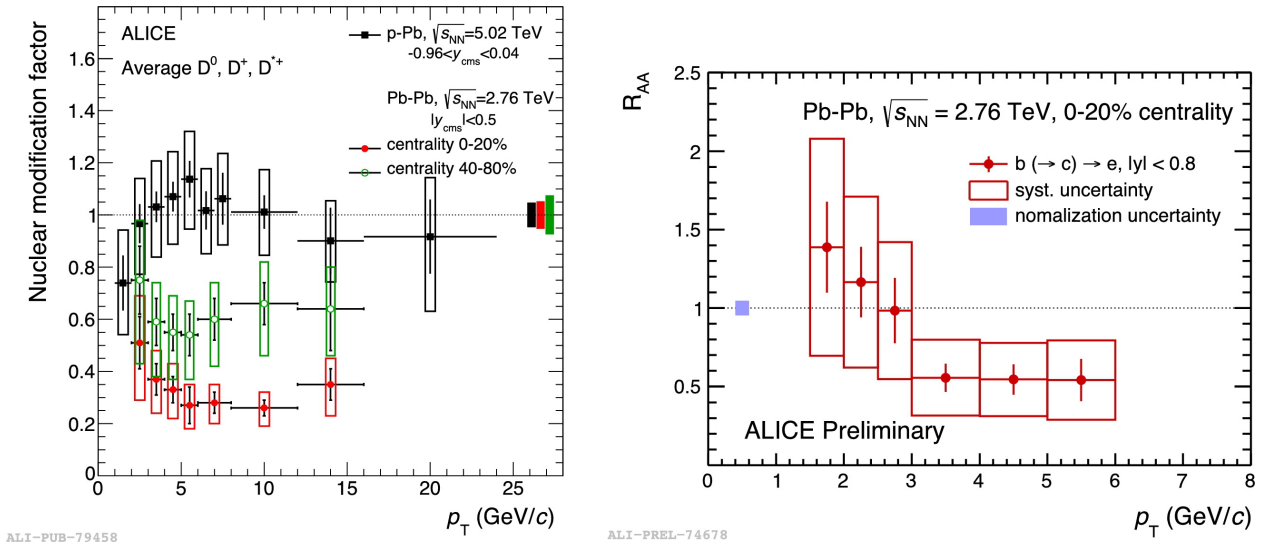Figure 6: Left panel: nuclear modification factor of average D mesons in p-Pb and Pb-Pb for central and semi-peripheral collisions [12]. Right panel: Suppression of electrons coming from beauty decays in Pb-Pb central collisions[12]

In this section a small extract of recent results shown at the 2014 Quark Matter Conference [12] is reviewed. Figure 6 shows the nuclear modification factor for prompt D^0 mesons for

the most central $(0 - 20\%)$ collisions and for semi-peripheral collisions $(0 - 40\%)$ in Pb-Pb for $\sqrt{s_{NN}} = 2.67$ TeV and for p-Pb collisions at $\sqrt{s_{NN}} = 5.02$ TeV. As predicted, one can see that the prompt D^0 are strongly suppressed in Pb-Pb collisions. Furthermore, the plot shows that the suppression depends on the centrality of the collision. The modification factor of prompt D^0 in p-Pb is close to unity. This indicates that the suppression is caused by the medium and thus is a final state effect, mainly caused by the charm energy loss. Figure 6 shows the nuclear modification factor for electrons coming from beauty decays, that are measured using the impact parameter separation method. It can be seen, that for $p_T > 3$ GeV/c there is a trend towards the suppression of the beauty electrons. The same measurement in p-Pb gave results close to unity, which also indicates that the suppression is a final state effect.
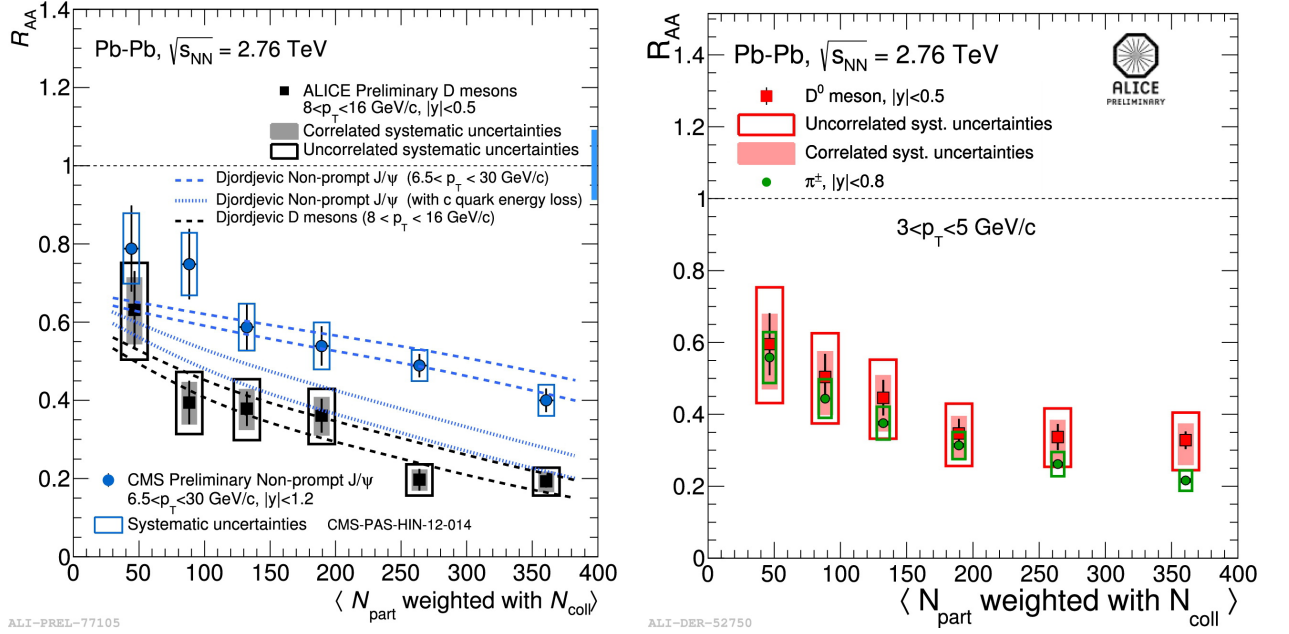

Figure 7: Left panel: Comparison of the centrality dependence of the nuclear modification factor of prompt D mesons measured in ALICE and J/ψ coming from beauty decays measured in CMS [12]. Right panel: centrality dependence of the nuclear modification factor of prompt D^0 mesons and charged pions [12]

In the left panel of figure 7 the centrality dependence of D mesons measured in ALICE and of J/ψ measured in CMS coming from beauty decays is compared. The p_T ranges are chosen in order to obtain the same average $p_T \approx 10$ GeV/c. The plot clearly shows, that the charmed mesons are stronger suppressed than the beauty mesons. Also the theoretical predictions are in good agreement with the measurements.

The right panel of figure 7 shows a comparison of R_{AA} of prompt D^0 mesons and charged pions depending on the centrality in a fixed p_T bin. Due to the large errors of the D^0 mesons, no statements about a stronger suppression of charged particles compared to charmed mesons can be made. Despite the qualitative considerations in the previous section, predictions of theory are in good agreement with the measurements. Considering the measurement strategies and the current results, it is clear that the precision of the primary vertex and the secondary vertex play a key role in the HF analysis. Thus one way to decrease the uncertainties in the measurements is to improve the precisions of the vertices. Besides detector

upgrades, this can be achieved by advanced reconstruction algorithms. A software that is dedicated for an improvement of the vertexing is the KFParticle vertexing package, developed by I. Kiesel, S. Gorbunov and now maintained by M. Zyzak at GSI whose performance will be the subject of this thesis.

4 The KFParticle Vertexing Package

This section is based on the PhD thesis of Sergey Gorbunov [13].

4.1 The Kalman Filter algorithm

The Kalman Filter algorithm provides an optimal estimate for a state vector and its covariance matrix from a set of measurements containing random variables (noise). The algorithm starts with an initial approximation of the state vector and the covariance matrix. Based on this approximation a prediction is made for the evolution of the state vector and the covariance matrix. By combining this prediction with a measurement a new, more precise, estimation for the state vector and its covariance matrix can be made. This is called the filtering step. Based on this a new prediction can be made and can be combined with the next measurement. This algorithm is repeated for all measurements. After the addition of the last measurement the obtained state vector and its covariance matrix is the best possible estimation.

4.2 Reconstruction of the primary vertex

The KF software [14] provides a fast reconstruction of the primary vertex using a set of track estimates and their covariance matrices that is suitable for a high-density track environment. Compared to conventional Kalman Filter vertex reconstruction, the KF uses an improved algorithm that simplifies the calculations significantly. The algorithm can be described as follows:

1. Set a first estimate of the position and the covariance matrix

2. Repeat the following fit several times:
   - Initialize the vertex state vector and covariance matrix from the previous iteration
   - Extrapolate the track candidate to the z coordinate of the vertex state vector
   - Calculate the χ^2 distance of the track from the vertex estimate
   - Calculate the parameters of the track at the vertex estimate
   - Update the vertex state vector with the Kalman Filter
   - Go on with next track

An important property of the fit of the primary vertex with the Kalman Filter is that it is possible to remove wrong measurements from the fit by subtraction of the measurement. This provides flexibility in order to correct the vertex fit for wrong assigned tracks.

4.3 Reconstruction of decayed particles

Many existing vertexing packages focus on the reconstruction of primary and secondary vertices. The KF software also provides an estimation of the parameters of the decayed particle [15], which means, that in general not only secondary vertices but all possible particles at their production vertices can be reconstructed from daughter estimates and their covariance
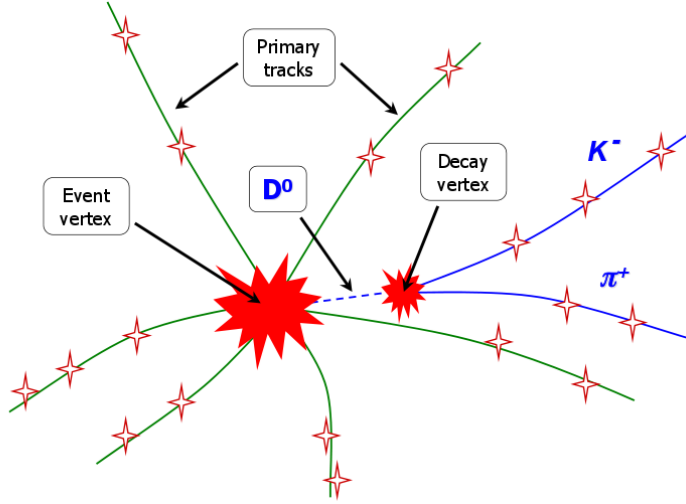
Figure 8: Schematic visualization of a D^0 decay [13]

matrices. A schematic example for the decay of a D^0 in a pion and a kaon can be seen in figure 8. The Kalman Filter algorithm was extended to properly take into account correlated errors of measurements. The state vector used for the Kalman Filter is the classical representation:

$$\boldsymbol{x^T} = (x, y, z, p_x, p_y, p_z, E, s) \tag{3}$$

The parameter s is added after the reconstruction of the decay vertex. It is defined as the length of the particle trajectory from the production to the decay vertex normalized by its momentum. By parametrizing the trajectory of the particle with the trajectory length normalized to the momentum, the particle can be transported to every point on its trajectory. Consequently by reconstructing the particle with KF the whole track of the particle is obtained. Differently from the ALICE track model (chapter 5), this makes the KF package independent from the geometry of the experiment. More physical parameters can be calculated after the fit, amongst them the momentum, the invariant mass and the proper decay time. The algorithm of the reconstruction of the particle parameters can be described as follows:

1. initial approximation of the coordinates of the secondary vertex

2. transport daughters to the initial vertex approximation

3. calculate the approximated momentum of the daughter and its covariance matrix at the approximated initial vertex position

4. Measurement of the state vector of the mother by the daughters according to the Kalman Filter formalism

5. Repeating of this procedure for all daughters

To achieve stability, this procedure is repeated several times.

4.4 Constrained fits

By making certain assumptions on the tracks, the precision of the fit described in the previous section can be improved. The constraints are treated by the Kalman Filter like one dimensional measurements added to the vertex fit.

4.4.1 The topological constraint

A topological constraint can be applied, when an hypothesis on the production vertex of the particle in question is available. In such a case it is assumed that the decayed particle originates from the production vertex. The fit is updated with the additional informations. In the case of a particle decaying close to the production or in the case of an uncharged particle, the vertex and the particle are approximately connected with a straight line:

$$\boldsymbol{v} - \boldsymbol{p} \cdot t = \boldsymbol{v_{PV}} \tag{4}$$

with $(\boldsymbol{v}, \boldsymbol{p})$ position and momentum of the particle and $\boldsymbol{v_{PV}}$ the position of the production vertex. From this it is clear that the particle trajectory is forced to point to the production vertex. The particle is transported to the production vertex and then gets filtered using the production vertex as a measurement. The errors of the primary vertex are also taken into account by the algorithm.

4.4.2 The mass constraint

If the invariant mass of the particle is known, the precision of the parameters can be further improved. The mass constraint takes the form:

$$M^2 = E^2 - (p_x^2 + p_y^2 + p_z^2) \tag{5}$$

This is used by the Kalman Filter as a one dimensional measurement.

4.5 Versions of KFParticle and motivation for a test

In general the software is under development for the CBM experiment, where it will become the main tracking and vertexing software, and is used in ALICE and in the STAR experiment. The version that is available in the ALICE framework AliROOT is called AliKFParticle. It is partially used for the reconstruction of V^0 decay topologies (chapter 2.4) as well as for some HF analyses. Moreover, in 2007 the AliKF was tested successfully. However, the AliKF is no longer maintained by the authors. A new, more developed, unified version for all experiments has been introduced, called KFParticle.

During first tests of this new version a serious problem with the estimation of the covariance matrix has been discovered in the context of this work. Since no tests of the algorithm are existing, neither for the AliKFParticle nor for the KFParticle, it became clear, that an extended use of this software in the ALICE experiment will only be possible after the verification of the implemented code that can be repeated after every update of this complex software. Therefore it was decided to develop an Unit Test for this vertexing package whose design is described in chapter 6. Since some parts of the AliKF have already been verified, this version is also tested to have a comparison to the performance of the new unified

version. For the use of this software in the physics analysis it is mandatory to switch to the new KFParticle version in order to have the possibility to get new needed functionalities implemented. For the heavy flavour analysis the full kinematic reconstruction of the mother, the two constraints and the possibility to improve the resolution of the primary vertex by adding the mother and removing the daughters are very powerful tools. New physics can be investigated with a reliable version of the KFParticle and thus the effort to write a Unit Test for this software is justified. For this test it is important to have a basic knowledge of the track model in ALICE which will be provided in the next section.

5 The ALICE Track Model

In the ALICE experiment the track reconstruction is based on the Kalman Filter algorithm. In the following an overview over the chosen coordinate systems and track parameters is given. It is shown how the parametrization is linked to the measurement and the errors of the parameters are discussed.

5.1 Equation of motion

In a homogeneous magnetic field without additional electrical field and material effects a particle has to satisfy the equation of motion according to the Lorentz force [16]:

$$\boldsymbol{F_L} \sim q\boldsymbol{v} \times \boldsymbol{B} \tag{6}$$

where q denotes the signed charge and $\boldsymbol{v}$ the velocity. In vacuum this gives the following equation of motion:

$$\frac{d\boldsymbol{p}}{dt} = \frac{d(m\gamma \cdot d\boldsymbol{x}/dt)}{dt} = c^2 \kappa q \boldsymbol{v}(t) \times \boldsymbol{B}(\boldsymbol{x}(t)) \tag{7}$$

Here $\boldsymbol{x}$ stands for a space point of the particle, κ has the meaning of a proportional factor depending on the choice of units, m denotes the rest mass, $\gamma = \sqrt{1/(1 - \beta^2)}$ the Lorentz-factor with $\beta = |\boldsymbol{\beta}| = |\boldsymbol{v}/c|$ and t gives the time in the laboratory frame.

It is possible to express this equation using geometrical quantities only. The equation of motion reads then:

$$\frac{d\boldsymbol{x}^2}{ds^2} = \frac{\kappa q}{p} \frac{d\boldsymbol{x}}{ds} \boldsymbol{B}(\boldsymbol{x}(s)) \tag{8}$$

where $s(t)$ denotes the path length of the trajectory with $ds/dt = v$ and $p = |\boldsymbol{p}| = |m\gamma\boldsymbol{\beta}c|$ the absolute value of the relativistic momentum in the laboratory frame.

Integrating this equation gives six parameters, but because of the identity:

$$(\frac{dx}{ds})^2 + (\frac{dy}{ds})^2 + (\frac{dz}{ds})^2 = 1 \tag{9}$$

one parameter can be chosen arbitrary and only five free parameters remain. The arbitrary choice of one parameter defines a reference surface for the trajectory.

For a homogeneous solenoidal magnetic field that goes along the z-axis $\boldsymbol{B} = B\boldsymbol{e_z}$, like in the ALICE experiment, the equation of motion is solved by a helix with an axis parallel to the z-axis. The choice of the free parameters depends on the set-up of the detector and the reconstruction strategy of the tracks. The consequences of the usage of the Kalman Filter for the track fit for the choice of the coordinate systems and the parametrization will be discussed in the following section.

5.2 Track parameters in ALICE

5.2.1 Description of the parametrization

The global coordinate system of ALICE has the following properties [6]:

- right handed and cartesian

- origin is at the ideal beam-beam interaction point in the central barrel

- Z-axis goes along the beam line

- X-axis points towards the centre of the LHC ring

- Y-axis is perpendicular to the $X - Z$ plane and points upwards

The main sub detectors for tracking in the central barrel of ALICE use a local coordinate system, that considers the partitioning of the subdetectors in sectors over the full azimuth for the ITS and the TPC. The local system can be obtained by rotating the global system around the Z-axis by an angle α, where α is the angle between the X-axis and the bisector of the sector that the track crossed. This implies the following properties for the local system:

- right handed

- X-axis is perpendicular to the sensitive plane of the respective subdetector

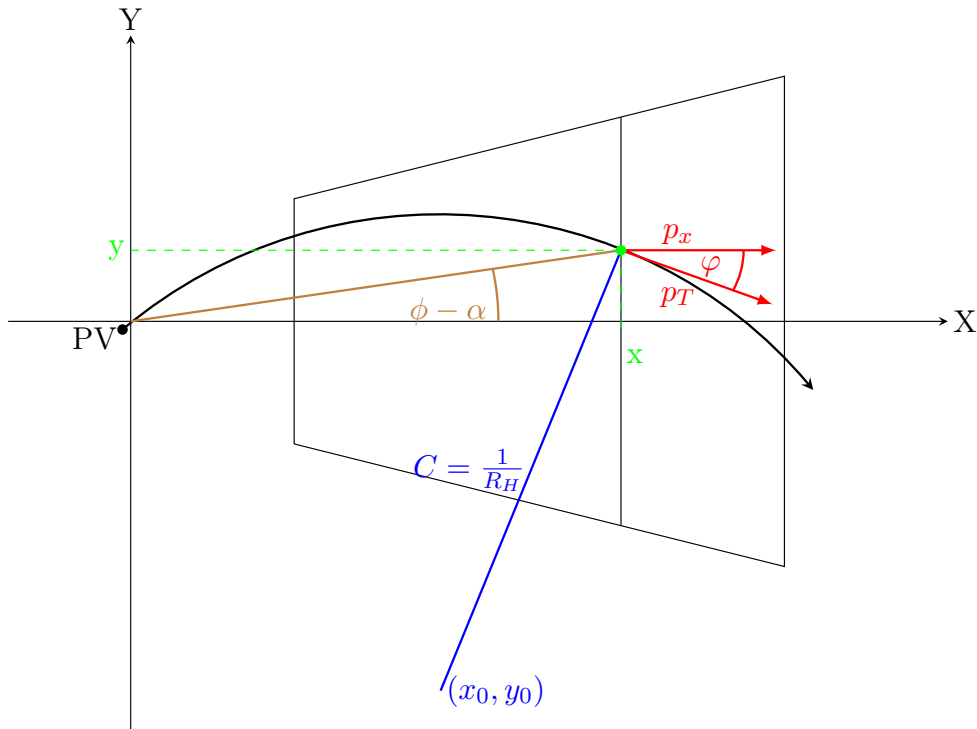- origin and Z-axis are the same as in the global system

Figure 9: Coordinate system of the TPC: reference plane x at the intersection between the pad plane and the X-axis. The sector is rotated around the angle α. Φ is the measured angle in the global system. The local inclination angle at the reference point x is denoted with φ, while C denotes the curvature. The figure is not in a realistic scale.

In the local frame the track is described at each point by the helix model. Consequently the track is characterized by a state vector with 5 parameters and a 5×5 covariance matrix.

The choice of the parameters for the Kalman Filter state vector is described in figure 9. The intersection point between the X-axis and the sensitive plane after the rotation defines the reference surface for the trajectory. This is denoted with the coordinate x. The y-coordinate of the track at a given reference plane x is then given by the solution of the helix equation depending on x [17]:

$$y(x) = y_0 - \frac{1}{C}\sqrt{1 - (Cx - \eta)^2} \tag{10}$$

and the solution for the helix equation for the z-coordinate of the track at a given reference plane X is:

$$z(x) = z_0 - \frac{\tan\lambda}{C}\arcsin(Cx - \eta) \tag{11}$$

These two equations determine the evolution of the trajectory depending on x. In these two equations C is the curvature of the projection of the particle trajectory on the XY plane. Given the radius R_H of the helix, the curvature can be calculated as:

$$C = \frac{1}{R_H} \tag{12}$$

The second parameter $\tan\lambda$ denotes the tangent of the dip angle between the track and the transverse plane and is given by:

$$\tan\lambda = \frac{dz}{ds} \tag{13}$$

The last parameter η has the meaning of an azimuthal angle φ between the direction of the transverse momentum and the x-axis, which is described further in the next section, and is defined as

$$\eta = x_0 C \tag{14}$$

where x_0, y_0, z_0 are the coordinates of the centre of the projection of the trajectory on the transverse plane with $z_0 \equiv z(x_0)$. At a given reference plane x, the track can then be fully described by y, z and the three parameters C, η and $\tan\lambda$. Therefore the chosen state vector is:

$$\boldsymbol{x^T} = \{y, z, C, \tan\lambda, \eta\} \tag{15}$$

The parameter C is more convenient than the parameter R_H, since the error on the curvature is Gaussian, even at high momenta, whereas the error on R_H is not [18]. Another important reason for this choice of the local coordinate system is that η is approximately zero which ensures that the helix equations are approximately linear. This is required by the Kalman Filter for the transport. The switch between the global and the local system is fast, since the transformation is a simple rotation around the z-axis. If a particle leaves the sector, the coordinate system is rotated again and the parameters of y, z and η are recalculated, while $\tan\lambda$ and C stay the same. In the next section it is shown, how the parameters of the state vector are linked to the position and momentum of the measurement.

5.2.2 Connection between parameters and measurement

In general a cluster measured by a Time Projection Chamber gives a radial coordinate R, an azimuthal angle ϕ and a position in the Z direction and thus gives a 3-dimensional coordinate ($X = R\cos(\phi)$, $Y = R\sin(\phi)$, Z). The full kinematic information of the track
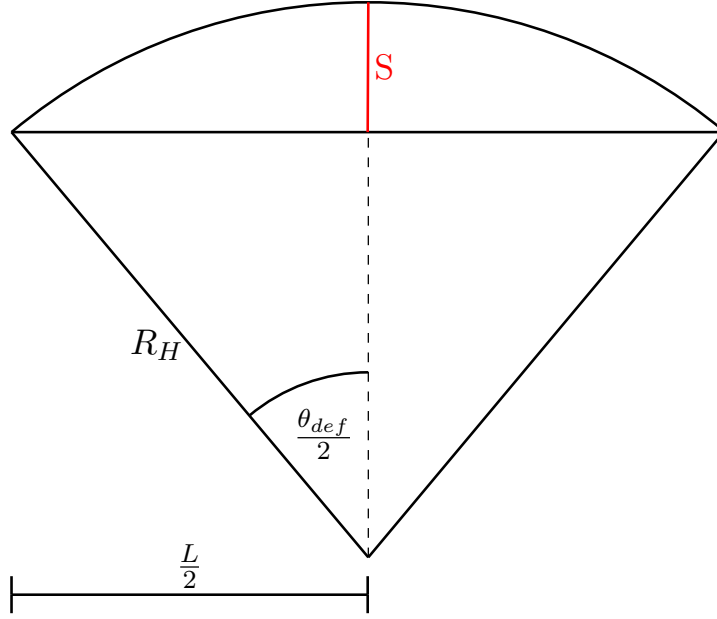
Figure 10: Sagitta S of a track: distance between the base and the centre of the resulting arc.

can be obtained by determining the transverse momentum, dip angle and the azimuthal angle of the track.

By combining at least 3 measured points, the curvature of the track can be calculated by evaluating the sagitta in the transverse plane. The sagitta of a track that is deflected in a magnetic is shown in figure 10. In the case of a particle moving in a magnetic field, the radius R_H of the helix projected on the transverse plane is related to the sagitta S via [19]:

$$S = R_H - R_H \cos \frac{\theta_{def}}{2} \tag{16}$$

where $\theta_{def} = \frac{L}{R_H}$ is the magnetic deflection angle and L the track length in the magnetic field projected on the transverse plane. Since R is usually large against L, θ_{def} can be approximated by: $\theta_{def} \approx \sin \theta_{def} = \frac{L}{R}$. Together with $1 - \cos\left(\frac{\theta_{def}}{2}\right) = 2 \sin^2\left(\frac{\theta_{def}}{4}\right)$ the following relationship between the sagitta and the radius R_H can be obtained:

$$S = \frac{L^2}{8R_H} \tag{17}$$

In the magnetic field the particle is deflected by the Lorentz force as given in equation 6. This force is equal to the centripetal force. In the transverse plane the transverse momentum $\boldsymbol{p_T}$ is perpendicular to the magnetic field. This leads to the following equation:

$$\frac{mv_T^2}{R_H} = \kappa q v_T B \tag{18}$$

Therefore the signed transverse momentum is linked to the radius R_H of the helix and therefore to the curvature by:

$$p_\mathrm{T} = \kappa q B R_H \tag{19}$$

Consequently by measuring the sagitta of the track the transverse momentum is given by:

$$p_{\mathrm{T}} = \frac{|\kappa q B| L^2}{8S} \tag{20}$$

and thus the curvature is proportional to the sagitta. The dip angle of the track, as illustrated

(a) 3-D illustration of the dip angle [20].

(b) Illustration of $\tan \lambda$ as the slope of the z co-ordinates as a function of the path length of the track in the transverse plane [19].
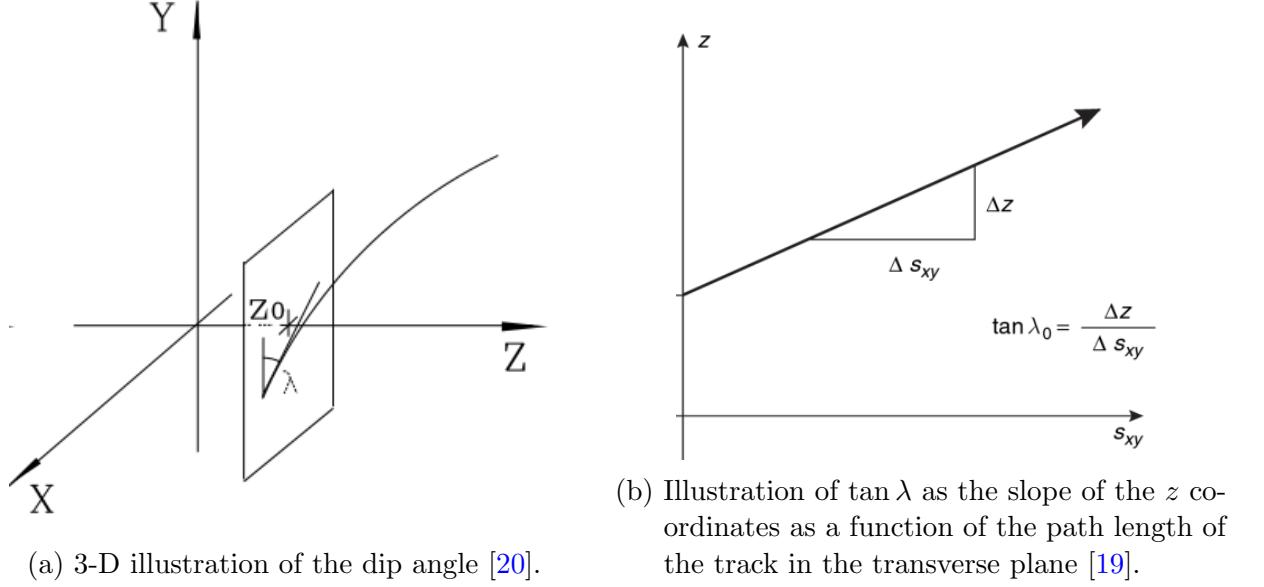
Figure 11

in figure 11a, is the angle between the transverse plane and the track. It can be obtained by from the z coordinates as a function of the path length of the track in the transverse plane (fig. 11b):

$$\lambda = \arctan\left(\frac{dz}{ds}\right) \tag{21}$$

It is often convenient to use the slope of the track $\tan \lambda$ in the $Z - XY$ plane. The slope is related to the direction of the track given by its momentum via:

$$\tan \lambda = \frac{p_z}{p_{\mathrm{T}}} \tag{22}$$

Using the dip angle of the track, it is possible to calculate the polar angle θ of the track:

$$\theta = \frac{\pi}{2} - \lambda \tag{23}$$

With the knowledge of θ the total momentum can be calculated as:

$$p = \frac{p_{\mathrm{T}}}{\sin \theta} \tag{24}$$

With this the values of p_T and p_z are defined. To obtain the values of p_x and p_y the azimuthal angle φ of the track, also shown in figure 9, is needed. Considering the circle equation in Cartesian coordinates, where x_0, y_0 and z_0 denote the coordinates of the centre of the circle:

$$(x - x_0)^2 + (y - y_0)^2 = R_H^2 \tag{25}$$

and comparing this to the equation in radial coordinates:

$$(R_H \sin \varphi)^2 + (R_H \cos \varphi)^2 = R_H^2 \tag{26}$$

gives the following expression for φ:

$$\varphi = \arcsin \frac{x - x_0}{R_H} \tag{27}$$

Here the sine of the φ angle gives the slope of the track in the transverse plane. It is related to the direction of the track via:

$$\tan \varphi = \frac{p_y}{p_x} \tag{28}$$

With this, the remaining components of the track momentum can be determined: $p_x = p_T \cos \varphi$ and $p_y = p_T \sin \varphi$. Consequently in an ideal TPC the kinematic variables x, y, z, p_x, p_y, p_z can be calculated in the local frame from a circle $(C, \sin \varphi)$ and a straight $(\tan \lambda)$.

5.2.3 Implementation of the parametrization

In the ALICE offline reconstruction the parameters of the tracks are estimated using a highly complex algorithm based on the Kalman Filter, because effects, for example caused by material and the electric field, have to be taken into account. The tracks are extrapolated to the primary vertex, where their parameters are stored. The parametrization in the local frame is implemented in the class AliExternalTrackParam in AliROOT. The state vector as implemented for the offline reconstruction [21] uses two parameters to specify the position: y and z at a reference plane x, two parameters to specify the direction: $\sin \varphi$ and $\tan \lambda$ and one parameter to quantify the sense of rotation and the magnitude of the momentum: $\frac{q}{p_T}$:

$$\boldsymbol{x^T} = \{y, z, \sin \varphi, \tan \lambda, \frac{q}{p_T}\} \tag{29}$$

This state vector is equal to the vector described in equation 15. This choice of the state vector ensures a fast transformation from the global to the local frame, which is important for the propagation of the tracks. Having the global coordinates of a track, the local position coordinates are immediately obtained by a rotation around the angle α:

$$x_{ref} = X \cos \alpha + Y \sin \alpha \tag{30}$$

$$z = -X \sin \alpha + Y \cos \alpha \tag{31}$$

$$z = Z \tag{32}$$

$$\sin \varphi = \sin \arctan^2 (p_y/p_x) \tag{33}$$

$$\tan \lambda = \frac{p_z}{p_T} \tag{34}$$

$$\frac{q}{p_T} = sign(\frac{1}{p_T}, q) \tag{35}$$

If the particles are propagated, the parameters have to be corrected for effects due to multiple scattering and energy loss in the material budget, as well as for other detector effects such as calibration and alignment.

5.3 Covariance matrix of the track parameters in ALICE

5.3.1 The covariance matrix

The covariance [22] of two random variables Cov(X,Y) provides information about the correlation between two sets of random variables X and Y. The covariance is defined by the expectation values:

$$Cov(X,Y) = <XY> - <X><Y> \tag{36}$$

where $<X>$ and $<Y>$ denote the mean values of X and Y respectively. Some important properties of the covariance matrix are:

- $Cov(X,Y) = 0 \Leftrightarrow$ increase of X does not affect Y $\rightarrow$ X,Y uncorrelated

- $Cov(X,Y) > 0 \Leftrightarrow$ increase of X implies increase of Y $\rightarrow$ X,Y correlated

- $Cov(X,Y) < 0 \Leftrightarrow$ increase of X implies decrease of Y $\rightarrow$ X,Y anticorrelated

- the covariance is a generalization of the variance:
  $Cov(X,X) = <X^2> - <X>^2 = Var(X,X)$

- the covariance is symmetric: $Cov(X,Y) = Cov(Y,X)$

In the following the symbol σ_X^2 will be used for the variance and the symbol σ_{XY} for the correlation of two sets of random variables X and Y. Since the correlation does not specify the strength of the dependence between two random variables, it is often convenient to use the correlation coefficient defined by:

$$\rho_{XY} = \frac{\sigma_{XY}}{\sqrt{\sigma_X^2 \sigma_Y^2}} \tag{37}$$

with the important property:

$$-1 \leq \rho_{XY} \leq 1 \tag{38}$$

With this property it is possible to make statements about the strength of the correlation between two variables. The covariance matrix C of an n-dimensional random vector X is a $n \times n$ matrix defined as:

$$C(X) = Cov(X_i, X_j) \tag{39}$$

Since the correlation between two random variables is symmetric, the covariance matrix is a symmetric matrix. By definition the covariance matrix contains the variance of the respective vector element on the diagonal and the correlations between the elements on the off diagonal elements.
This means that the 5x5 covariance matrix of the 5 dimensional state vector contains the errors of the track measurement and the correlation between the parameters.
There are two main contributions that dominate the error of the track: the error of the track caused by the detector resolution and the error coming from multiple scattering and energy loss in the material budget. In the following these processes and their impact on the elements of the covariance matrix will be discussed briefly.

5.3.2 Track error caused by the detector

The detector measures the $R\phi$ and the z coordinate precisely and therefore the transverse momentum p_T. The uncertainty of the measurement on the position comes from the spatial resolution of the detector [16]. Since the transverse momentum is measured by the deflection in the magnetic field, the resolution of the transverse momentum $\frac{\sigma_{p_T}}{p_T}$ depends on the precision of the deflection measurement, which is the error of the sagitta of the track and therefore:

$$\frac{\sigma_{p_T}}{p_T} = \frac{\sigma_S}{S} \tag{40}$$

The measurement error of the sagitta depends on the errors of the spatial measurement by error propagation. In the simplest case of 3 measured points (x_1, x_2, x_3) that are placed at the beginning, center and end of the magnet giving the error $\sigma_{R\phi}$, the sagitta can be calculated as:

$$S = x_2 - \frac{x_1 + x_3}{2} \tag{41}$$

and its error:

$$\sigma_S = \sqrt{\frac{3}{2}}\sigma_{R\phi} \tag{42}$$

From this one can calculate the transverse momentum resolution:

$$\frac{\sigma_{p_T}}{p_T} = \frac{\sigma_S}{S} = \frac{\sigma_{R\phi}}{|\kappa q B|L^2} \cdot 8p_T \tag{43}$$

In the simplest case the track errors on the slopes can be calculated from the errors on a line through two points.

In the more general case, having N equidistant measured points of a track with projected track length L, the resolutions of the track parameters are approximately given by the Glückstern formulas in the asymptotic limit for large N. As shown by R. Glückstern [23] it is possible to calculate the track errors from a least squares fit. In the transverse plane these formulas assume a least squares fit of a parabola to obtain the errors on the direction $\sin\varphi$ and on the curvature C:

$$y = \alpha + \sin\varphi x + Cx^2 \tag{44}$$

where α is a constant. Calculating the RMS of the fit parameters and considering that for C and $sin\varphi$ only $\sigma_{R\phi}$ contributes, one gets in the asymptotic limit for the curvature and thus for $\sigma_{\frac{1}{p_T}}$

$$\sigma_{\frac{1}{p_T}} = \frac{\sigma_{R\phi}}{|\kappa q B|L^2}\sqrt{\frac{720}{N+5}} \tag{45}$$

and for the direction $\sin\varphi$

$$\sigma_{\sin\varphi} = \frac{\sigma_{R\phi}}{L}\sqrt{\frac{192}{N+4.9}} \tag{46}$$

where L is the track length projected in the transverse plane. For the error on $\tan\lambda$ the Glückstern formulas calculate the RMS of a linear fit. It is assumed, that the error on the slope of the dip angle only depends on $\sigma(z)$. Calculating the RMS gives:

$$\sigma_{\tan\lambda} = \frac{\sigma_z}{L}\sqrt{\frac{12N}{(N+1)(N-1)}} \tag{47}$$

where here L denotes the track length projected in the z direction.

5.3.3 Track error caused by multiple scattering

A charged particle crossing matter interacts with nuclei and electrons [19]. By scattering on the Coulomb fields of them, the particle is deflected from the path predicted by the equation of motions in vacuum. The single scatterings are statistically independent from each other. Therefore by traversing the material of a detector, the particle undergoes a large number of scatterings and each time gets deflected by a small angle. The distribution of the scattering angles for the Coulomb scattering can be described by the Molière's theory of Coulomb scattering. This theory states, that for small scattering angles the angles are normal distributed around the mean value $\theta = 0$. The RMS for the scattering projected in two dimensions can be approximated as:

$$\theta_{RMS}^{proj} = \frac{13.6 MeV}{\beta c p} z \sqrt{\frac{x}{X_0}} [1 + 0.038 \ln{(\frac{x}{X_0})}] \tag{48}$$

with momentum p, velocity βc, charge of scattered particle z and x/X_0 the thickness of the medium in units of radiation length:

$$X_0 = \frac{A}{4\alpha N_A Z^2 r_e^2 \ln{(183 Z^{-1/3})}} \tag{49}$$

where Z is the atomic number and A the atomic weight of the absorber material, r_E the classical electron radius, N_A the Avogadro number and α the fine structure constant.
This equation can be further approximated by setting the charge $z = 1$ and multiplying with a factor of $\sqrt{2}$ to obtain the RMS in 3 dimensions:

$$\theta_{RMS}^{space} = \frac{19.2 MeV}{\beta c p} \sqrt{\frac{x}{X_0}} \tag{50}$$

Since β itself has a p_T dependence:

$$\beta = \frac{p}{\gamma m} \tag{51}$$

the multiple scattering is proportional to $\frac{1}{p_T}$ in the high momentum limit and proportional to $\frac{1}{p_T^2}$ in the low momentum limit.

5.3.4 Track error caused by energy loss

If a particle transverses material it loses energy according to the Bethe-Bloch formula, and thus changes the momentum of the particle. This gives an additional contribution to the error of the transverse momentum respectively the curvature. Once the particle is relativistic ($\beta\gamma \approx 4$), the energy loss is approximately constant, as can be seen in figure 12 and therefore also the uncertainty of the transverse momentum due to energy loss is approximately constant. By measuring the curvature of the track, $C = const \cdot \frac{1}{p_T}$ the error of it is given by:

$$\sigma_C = \sigma_{\frac{1}{p_T}} = \frac{d(\frac{1}{p_T})}{d(p_T)} \sigma_{p_T} = \frac{1}{p_T^2} \sigma_{p_T} \tag{52}$$

Therefore, in first order the energy loss is approximately contributing to $\sigma_{\frac{1}{p_T}}^2$ with $(\frac{1}{p_T^2} \sigma_{EL})^2$, where σ_{EL} is a constant.
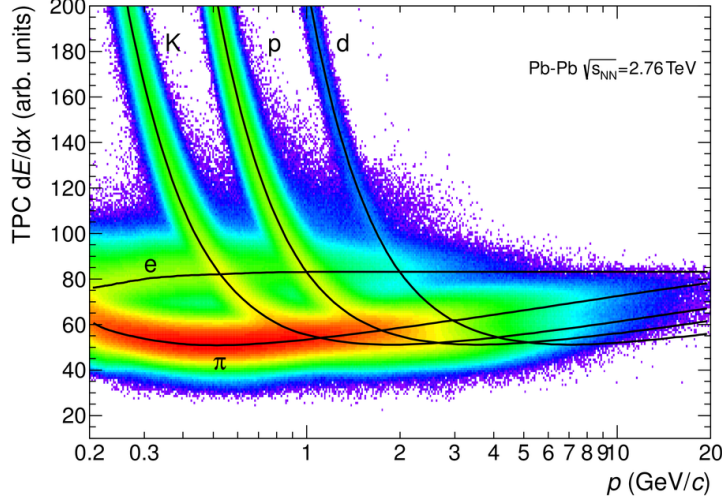
Figure 12: Energy loss signal in the TPC. The lines show the detector response parametrized according to Bethe-Bloch [6].

5.3.5 Covariance matrix of the ALICE track parameters

As shown in the previous considerations, the covariance matrix elements depend on p_T in first order. Thus the total error of the track parameters is given in a first order approximation by:

$$\sigma_i = \sqrt{\sigma_{track}^2 + (\frac{1}{p_T\beta}\sigma_{MS})^2} \tag{53}$$

for $i = y, z, \sin\varphi, \tan\lambda, \frac{q}{p_T}$ and constant σ_{track} and σ_{MS}.

Moreover, all five parameters depend on θ: the larger the θ angle is, the more time spends the particle in material and therefore undergoes more multiple scattering. The exact θ dependence of the parameters is complex and is reviewed in [24]. As shown in the previous section, the error on $\frac{q}{p_T}$ is also depending on the energy loss, that is approximately scaling with $\frac{1}{p_T^2}$.

For the correlations of the parameters it can be shown, that the parameters in the transverse plane $y, z, \frac{q}{p_T}$ and the parameters in the z plane $z, \tan\lambda$ are approximately uncorrelated, which means that there are only four independent correlated entries remaining: $\sigma_{y,\sin\varphi}, \sigma_{y,\frac{q}{p_T}}, \sigma_{\sin\varphi,\frac{q}{p_T}}$ and $\sigma_{z,\tan\lambda}$. So the final covariance matrix with non zero elements is given by:

$$C = \begin{pmatrix} \sigma_y^2 & 0 & \sigma_{y,sn\varphi} & 0 & \sigma_{y,\frac{q}{p_T}} \\ 0 & \sigma_z^2 & 0 & \sigma_{z,tn\lambda} & 0 \\ \sigma_{y,sn\varphi} & 0 & \sigma_{sn\varphi}^2 & 0 & \sigma_{sn\varphi,\frac{q}{p_T}} \\ 0 & \sigma_{z,tn\lambda} & 0 & \sigma_{tn\lambda}^2 & 0 \\ \sigma_{y,\frac{q}{p_T}} & 0 & \sigma_{sn\varphi,\frac{q}{p_T}} & 0 & \sigma_{\frac{q}{p_T}}^2 \end{pmatrix} \tag{54}$$

Since all the parameters are affected by multiple scattering, all correlations are also expected to depend on multiple scattering. The correlations of $\sigma_{y,\sin\varphi}$ and of $\sigma_{z,\tan\lambda}$ are expected to be strongly anticorrelated. This can be seen in figure 13 in the simplest case of a track defined by only two points. Increasing the value of the measured point decreases the slope $\sin\varphi$ and

vice versa, which is per definition an anticorrelation. Therefore the value of the correlation coefficients for $\sigma_{y,\sin\varphi}$ and of $\sigma_{z,\tan\lambda}$ are expected to converge against -1.
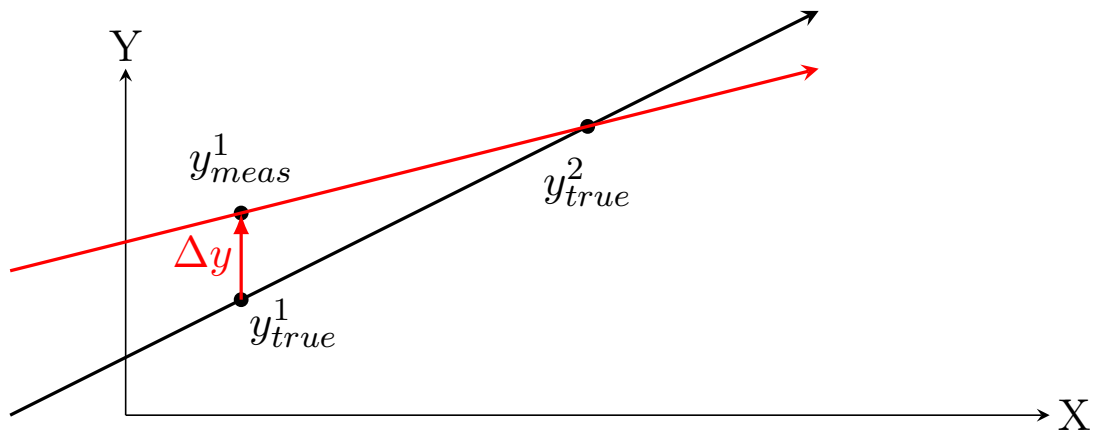

Figure 13: Anti correlation between y and the slope of the track ($\sin\varphi$) in the simplest case of a straight track defined by two point. Increasing the value of y^1_{true} decreases the slope of the track.

6 The Unit Test

6.1 The importance of Unit Tests

The used algorithms in the tracking and in the reconstruction of vertices contain advanced mathematical formalisms. To assure the quality of the software it is necessary to verify the correctness of the code. This is crucial for the analysis of the real data, since tracks and vertices are needed in almost every physics analysis. To verify the software, the code has to be tested on ideal simulations in order to have full control over the input. This is the only way to predict the result of the output and to see whether the functionalities of the code provide correct output. In the case of a unit test for a vertexing package this implies that in the ideal simulation all complications and detector effects, that are taken into account by the full reconstruction, are neglected and all processes are simulated Gaussian.

6.2 Design

The goal of this unit test is to test the functionality of the KF Package and to provide a benchmark for the performance of the KF in the ideal toy Monte Carlo (MC) case. Particles are generated in a pure kinematic simulation where the physics description of proton proton collisions is provided by PYTHIA [25]. This thesis deals with the charmed decay and its charge conjugate:

$$D^0 \rightarrow \pi^+ + K^- \tag{55}$$
$$\tag{56}$$

On a later stage it is planned to investigate the following strange decays:

$$\Lambda^0 \rightarrow \pi^- + p^+ \tag{57}$$
$$K_s^0 \rightarrow \pi^+ + \pi^- \tag{58}$$

In order to simulate tracks with the generated particles, the particles have to be smeared. To get a realistic smearing, assumptions about the covariance matrix, that describes the errors and the correlations of the parameters, have to be made. It is assumed that a parametrization of the distribution of the covariance matrix elements from old ALICE data can be used to smear the ideal MC parameters according to a Gaussian distribution with the precision of this covariance matrix. This process is called a fast simulation. Since some of the parameters in the ALICE track model are correlated, this has to be taken into account in the smearing. This can be done by using an algorithm called Cholesky decomposition. In the following the single steps of the fast simulation are outlined:

1. Generation of proton-proton event with PYTHIA

2. Creation of ideal tracks in the ALICE track model

3. Smearing and correlation of the parameters according to a given parametrized covariance matrix using a Cholesky decomposition

4. Creation of realistic tracks in the ALICE track model with the smeared particle parameters and the parametrized covariance matrix.

After the fast simulation, the mother is reconstructed using different vertexing methods. On a later stage it is planned to also smear the covariance matrix and to test the KF with real data.

6.3 Generation of the particles

The particles are generated using Pythia 6.2. A centre of mass energy of $\sqrt{s_{NN}} = 7$ TeV is used. The settings of the process are chosen in order to enhance the production of charm. All D^0 are forced to decay in the $K^- + \pi^+$ channel and the charge conjugates. Moreover only decays in the central barrel part of the ALICE detector $45\,° < \theta < 135\,°$ are chosen. The magnetic field is set to zero. In general it is possible to create arbitrary high statistics.

6.4 Extraction of the parametrization
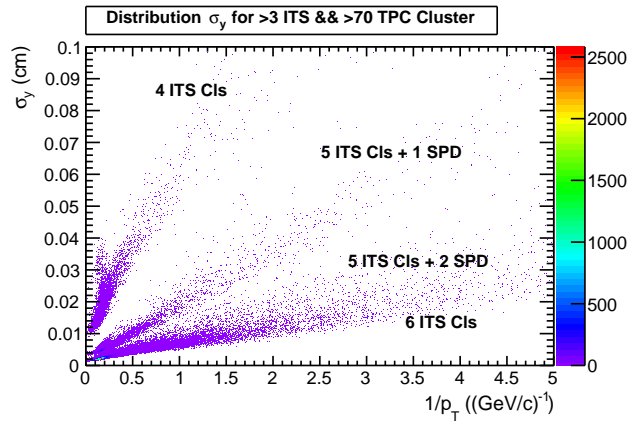
Figure 14: Distribution of σ_y of tracks from the sample LHC13b depending on the hits in the ITS as a function of p_{T}

Since the kinematic MC simulation gives ideal parameters, it is necessary to make assumptions about the errors of the ideal parameters. In this work the parametrization for the covariance matrix is extracted from real filtered ALICE data. The used filtered data are lead-proton interactions from the sample LHC13b. As can be seen in figure 14 the values of the covariance matrix depend strongly on the number of clusters in the ITS. In figure 14 are roughly 3 distributions visible: The structure with the lowest errors is a convolution of tracks with 6 ITS clusters and 5 ITS clusters with 2 hits in the first two layers of the ITS. The second structure originates mostly from tracks with 5 ITS clusters and only one hit in the Silicon Pixel Detectors and the third structure with the highest error is originating from tracks with 4 ITS cluster. Moreover, for all structures a dependence on the inverse transverse momentum is visible. Therefore the covariance matrix elements are parametrized in $\frac{1}{p_{\mathrm{T}}}$. As can be seen in the following sections there are more dependencies on other parameters, which are not taken into account in this first approach of the parametrization. In this work the parametrization for tracks with 6 ITS clusters and at least 70 TPC clusters is extracted.

6.4.1 Diagonal elements

The square root of the diagonal covariance matrix elements is plotted against $\frac{1}{p_T}$ for each track. At the moment no difference between the different particle species is made. With the pre-considerations done in chapter 5.3, the following power law depending on $\frac{1}{p_T}$ is chosen as fit function for the parameter errors:

$$\sigma_i = \sqrt{\sigma_{track}^2 + \sigma_{MS}^2 \cdot \left| \frac{q}{p_T} \right|^\alpha} \tag{59}$$

for $i = y, z, \sin\varphi, \tan\lambda, \frac{q}{p_T}$. The exponent in the multiple scattering term takes into account the p_T dependence of $\frac{1}{\beta}$.

The distribution of σ_y is shown in a scatter plot in figure 15a. The fit of the distribution is done from the profile of the scatter plot, shown in figure 15b. This means that the x-axis of the scatter plot is partitioned in bins and for each bin the mean value of the scattered points is computed.
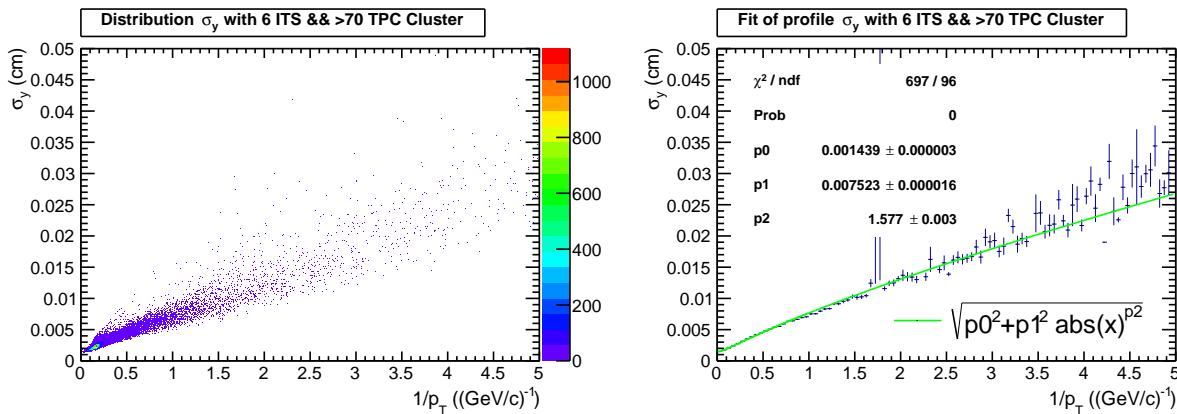
(a) Distribution of σ_y depending on $\frac{1}{p_T}$ in real ALICE data.

(b) Fit of the profile of the scatter plot of σ_y.

Figure 15

To have a check of the quality of the parametrization, the residuals of the fit are plotted (fig. 16a). The residuals are obtained by dividing the original value for the covariance matrix element for each track by the fitted value. It can be seen that the residuals of the first diagonal element are distributed around the expected value 1 with RMS of about 10 %. This shows that good agreement between fast simulation and data is achieved.

The spread in the distribution of the covariance elements comes from the neglected dependence on η. One possible reason for the asymmetry in the residuals for high-p_T is the φ dependence of the errors caused by the blind regions of the TPC, called Edge effect. If a particle leaves a TPC sector, it crosses a blind region of the TPC and gets fewer clusters assigned. Thus it error increases. This can be seen in figure 16b. Here the tangent of the φ angle times the charge is plotted against σ_y of the TPC standalone tracking for tracks with $p_T > 2$ GeV/c. By multiplying with the charge all tracks leaving the sector appear in the right bins and all tracks that come from blind regions and continue in the shown TPC sector appear in the left bins. Therefore an asymmetry between the left and the right side
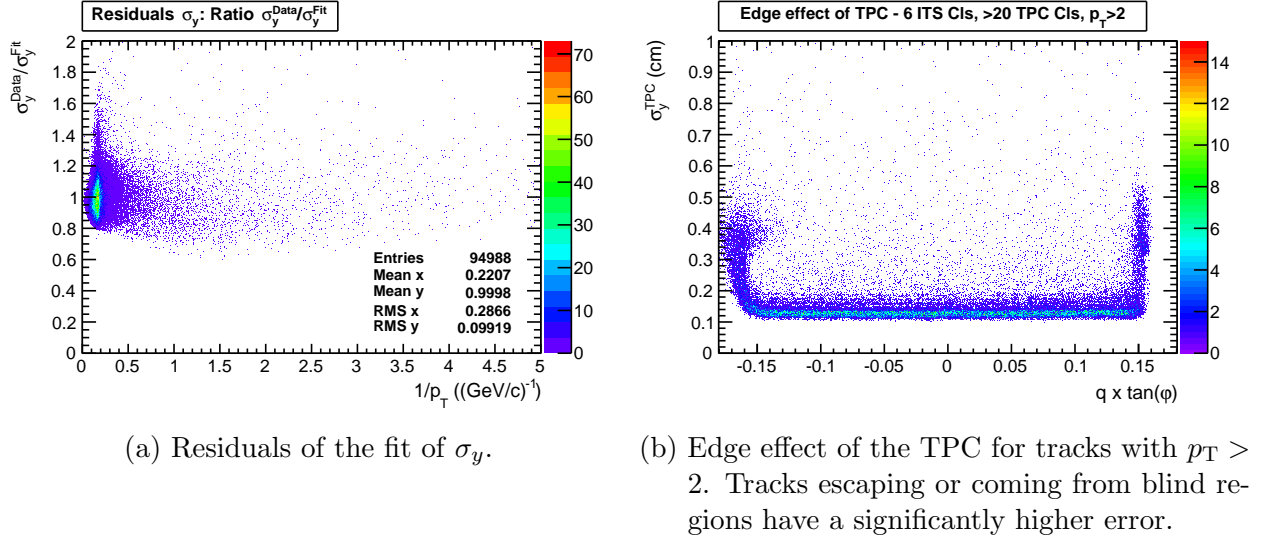
(a) Residuals of the fit of σ_y.

(b) Edge effect of the TPC for tracks with $p_T >$ 2. Tracks escaping or coming from blind regions have a significantly higher error.

Figure 16

can be seen. In general a significant increase in the errors for particles leaving or coming from blind regions can is visible. The behaviour of the distribution and the residuals of the fits are qualitatively the same for $\sigma_z, \sigma_{\sin\varphi}$, and $\sigma_{\tan\lambda}$.

As described in the previous chapter, for $\frac{q}{p_T}$ also energy loss contributes to the uncertainty in the low p_T region. However, to have a test in the ideal case it is assumed that the material is homogenous and thus the energy loss is neglected, although it is simple to make a correction for it by adding a term proportional to $(\frac{1}{p_T})^2$. The distribution and the fit is shown in figure 17a and 17b. The residuals (fig. 18) show that the uncertainty in the low-p_T region
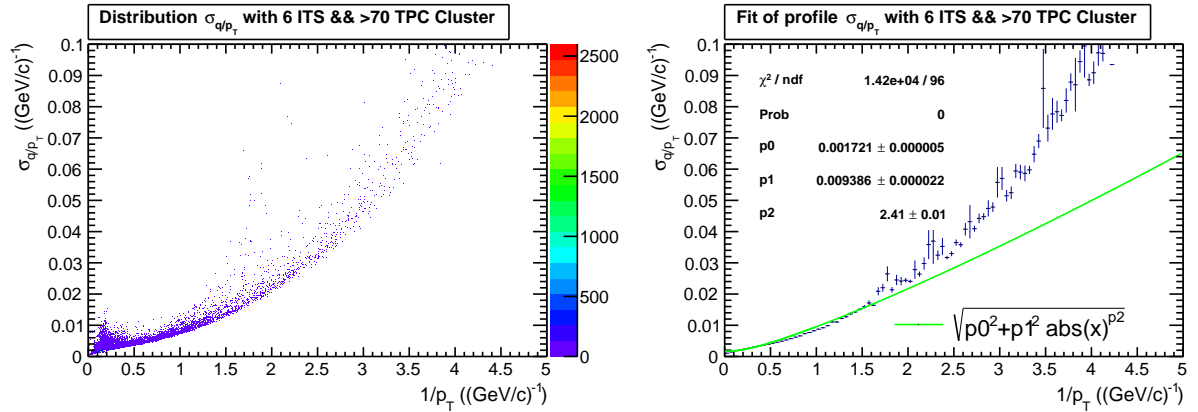
(a) Distribution of the uncertainty of $\frac{q}{p_T}$ depending on $\frac{1}{p_T}$ in real ALICE data.

(b) Fit of the profile of the scatter plot of $\frac{q}{p_T}$ neglecting energy loss.

Figure 17

is underestimated. In the high-p_T region of the $\frac{q}{p_T}$ distribution a strong structure is visible. The origin of this structure is the material in the TPC. Again effects from the edges play an important role. Therefore the high p_T region is not well described by the fit. The RMS is 17 % and the mean value is 0.99. However, the quality of this fit is good enough to provide
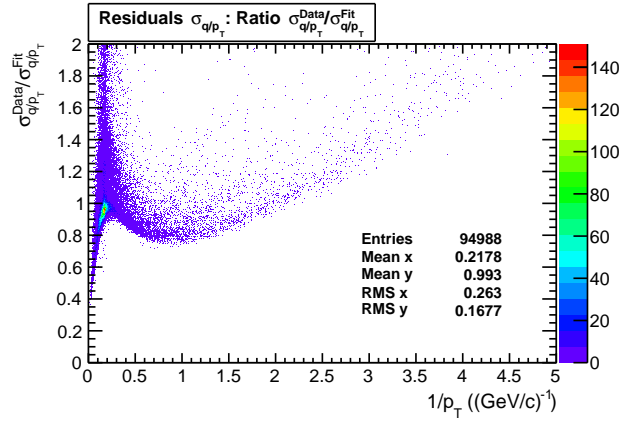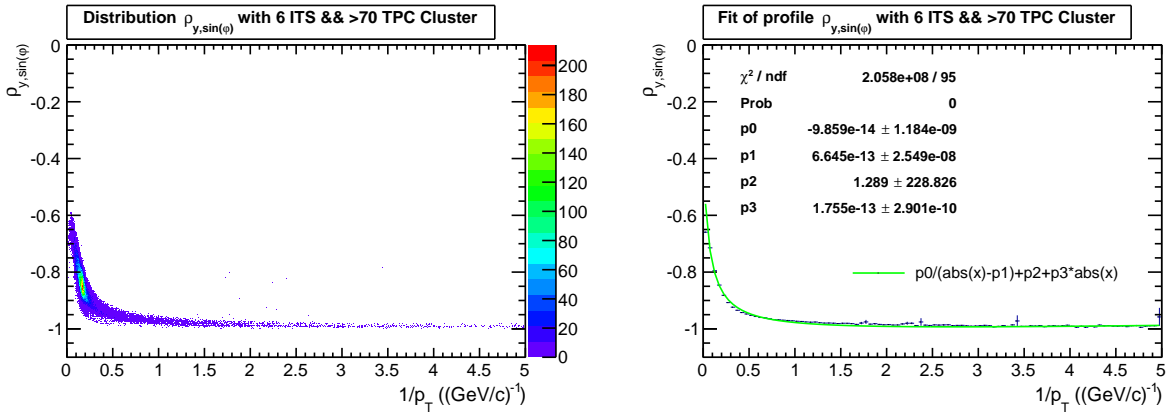
realistic input for the unit test.

Figure 18: Residuals of the fit of $\sigma_{\frac{q}{p_T}}$.

6.4.2 Off-diagonal elements

For the off-diagonal elements the correlation coefficients are plotted against $\frac{1}{p_T}$. The fit functions are guessed. Optically the distribution of $\rho_{y,\sin\varphi}$ in figure 19a behaves like a hyperbola. Therefore the following fit function is chosen:

$$\rho_{y,\sin\varphi} = \frac{A}{abs(x) - B} + C + \sigma_{MS} \cdot abs(x) \tag{60}$$

(a) Distribution of the correlation coefficient $\rho_{y,\sin\varphi}$ as a function of $\frac{1}{p_T}$.

(b) Fit of the profile of the scatter plot of $\rho_{y,\sin\varphi}$ with a hyperbola and a multiple scattering term.

Figure 19

As expected, the distribution converges to -1 for low transverse momenta. This is not true any more for the high-p_T tracks. The reason for this behaviour is the fact that for the low-p_T tracks the multiple scattering in the first layers of the ITS is the dominating effect. The
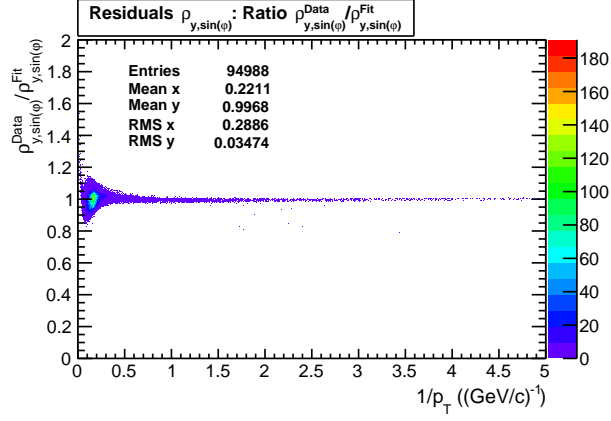
Figure 20: Residuals of the fit of $\rho_{y,\sin\varphi}$.

particles position is strongly influenced by a change of the direction due to the scattering. However, for high-p_T tracks more effects than multiple scattering influence the track and thus the correlation between the position and direction in the transversal plane decreases. As for the diagonal elements, the profile of the scatter plot is fitted (fig. 19b). The residuals are shown in figure 20. They indicate that the distribution is well described by the fit. The RMS is 3.5 % and the mean value 0.99. The same holds for the distribution of $\rho_{z,\tan\lambda}$. The distribution of $\rho_{\sin\varphi,\frac{q}{p_T}}$ is also fitted with a hyperbola and a multiple scattering term (fig. 21a).

$$\rho_{\sin\varphi,\frac{q}{p_T}} = \frac{A}{-abs(x) - B} + C + \sigma_{MS} \cdot abs(x) \tag{61}$$
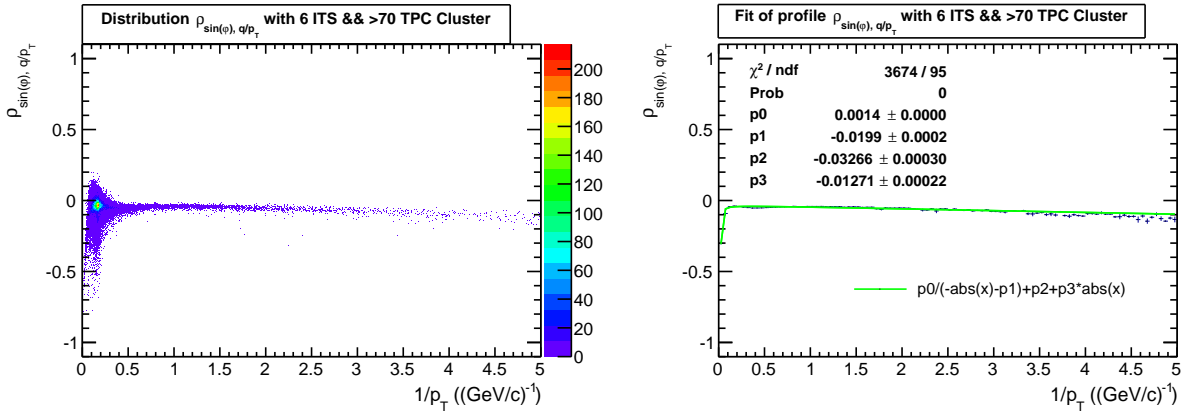
(a) Distribution of the correlation coefficient $\rho_{\sin\varphi,\frac{q}{p_T}}$ as a function of $\frac{1}{p_T}$.

(b) Fit of the profile of the scatter plot of $\rho_{\sin\varphi,\frac{q}{p_T}}$ with a hyperbola and a multiple scattering term.

Figure 21

For the mid- and the low-p_T, the correlation is dominated by multiple scattering and is small. In the high-p_T region the spread is very high. This reflects in the residuals in figure 22. The mean value is shifted and the RMS is 44 %. Reasons for this asymmetric behaviour
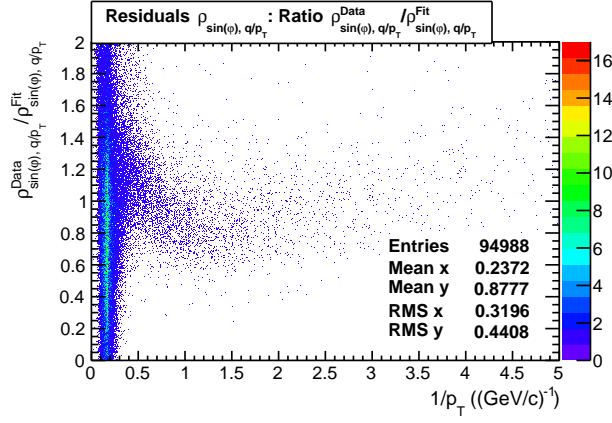
40

Figure 22: Residuals of the fit of $\rho_{\sin\varphi, \frac{q}{p_T}}$.

are probably the structures seen in the distribution of $\sigma_{\frac{q}{p_T}}$. The same behaviour is seen for the remaining non-zero covariance element $\rho_{\tan\lambda, \frac{q}{p_T}}$.

6.5 Smearing of the parameters

The smearing of the particles is done using a Cholesky decomposition [22]. Any symmetric positive-definite matrix C can be uniquely expressed as:

$$C = U^T U \tag{62}$$

where U denotes a real upper triangular matrix, that has positive diagonal elements. The Cholesky decomposition is numerical stable and provides an efficient calculation of the decomposed matrices. Multiplying an uncorrelated vector of random numbers with the triangular matrix results in a vector, that has the same properties like the matrix C [26]. Since the covariance matrix is symmetric and positive definite, every covariance matrix can be decomposed. Thus, having a covariance matrix C, the covariance properties of C can be resampled by generating a vector with random uncorrelated elements $\boldsymbol{x_{uncorr}}$ and multiplying it with the transposed decomposed matrix:

$$\boldsymbol{x_{corr}} = U^T \boldsymbol{x_{uncorr}} \tag{63}$$

It depends on the implementation of the algorithm whether the transposed matrix U^T or the untransposed matrix U is used. To make the procedure of the smearing clearer, an example will be given in the following section.

6.6 Example of the generation of a smeared particle track

To explain the single steps of the fast simulation described in section 6.2 a negatively charged Monte Carlo kaon (K^-) generated by PYTHIA is considered:

```
152 TParticle: K-   p: 0.970260 -1.189899 -3.763413
                    Vertex: 2.429979e-03 -4.672045e-03 -2.880410e-02   64
```

coming from a D^0 decay:

```
64 TParticle: D0     p: 0.637461 -1.225626 -7.556230
                     Vertex: 0.000000e+00 0.000000e+00 0.000000e+00     13
```

where the first number denotes the MC label, p the momentum, Vertex the production vertex and the last number the label of the mother particle. As can be seen here, the MC primary vertex position is always (0,0,0). By calling the constructor of the AliExternalTrackParam, the parameters of the MC particle are transformed into the parameters of the local coordinate system of the TPC:

```
AliExternalTrackParam: x = 0.0051565     alpha = -0.886727
  parameters:   -0.00106926 -0.0288041 7.23113e-17 -2.45119 -0.651322
```

The order of the parameters corresponds to $(y, z, \sin\varphi, \tan\lambda, \frac{q}{p_{\mathrm{T}}})$. As described in section 5.2.3 the value of z is unchanged, while the value of $\sin\varphi$ is very small, as required by the Kalman Filter. Since the parametrization is done with track parameters stored at the primary vertex, the ideal AliExternalTrackParam of the particle are propagated to the distance of closest approach to the primary vertex:

```
AliExternalTrackParam: x = 0              alpha = -0.886727
  parameters:   -0.00106926 -0.0161645 -3.8711e-17 -2.45119 -0.651322
```

Here the particle gets assigned a parametrized covariance matrix depending on its p_{T}. For this the absolute values of the fitted correlation coefficients are recalculated with :

$$\sigma_{i,j} = \rho_{i,j} \cdot \sigma_i \sigma_j \tag{64}$$

Next a vector with random numbers is generated. The random numbers of the vector are generated according to a Gaussian distribution with mean $= 0$ and $\sigma = 1$:

```
random vector    1.46539   -0.710064   -0.23887   0.971615   -0.276362
```

Then the assigned covariance matrix is decomposed using the Cholesky decomposition, which results in the following triangular transposed matrix:

```
5x5 matrix is as follows
   0.005554            0            0            0            0
          0       0.0143            0            0            0
  -0.001342            0    0.0004041            0            0
          0    -0.001624            0       0.0011            0
  0.0001459            0     -0.00024            0     0.005098
```

and the correlated random vector is obtained by multiplication with this matrix, which gives the following vector:

```
correlated random vector  0.008139 -0.01015 -0.002063 0.00222 -0.001137
```

This provides smoothly distributed Gaussian errors. The resulting correlated vector is added to the ideal parameters and together with the assigned covariance matrix random generated correlated AliExternalTrackParam are constructed at the DCA to the primary vertex. In case of the K- this looks as follows:

```
AliExternalTrackParam: x = 0                    alpha = -0.886727
   parameters:  0.00707018 -0.0263203 -0.00206316 -2.44897 -0.65246
   covariance:  3.085e-05
                        0  0.0002045
               -7.452e-06          0  1.964e-06
                        0 -2.322e-05          0  3.846e-06
                8.103e-07          0 -2.928e-07          0  2.607e-05
```
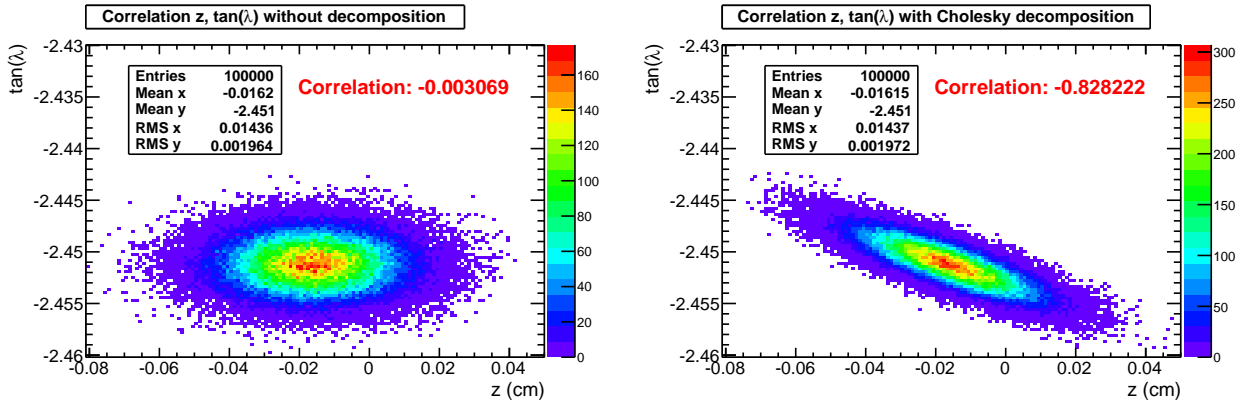
By calculating all correlation coefficients one gets the parametrized normalized covariance matrix:

```
Parametrized normalized covariance matrix:
5x5 matrix is as follows


         |       0   |       1   |       2   |       3   |       4   |
    --------------------------------------------------------------------
    0 |           1           0     -0.9575           0      0.02857
    1 |           0           1           0     -0.8278           0
    2 |     -0.9575           0           1           0     -0.04091
    3 |           0     -0.8278           0           1           0
    4 |      0.02857           0     -0.04091           0           1
```


(a) Example for a random Gaussian smearing without correlation.

(b) Example for a random correlated Gaussian smearing using a Cholesky decomposition.

Figure 23

As a cross-check whether the parameters are correlated according to the input parameters, 100.000 random correlated AliExternalTrackParam are generated from the example K-. To compare the effect of the multiplication with the decomposed matrix, the same smearing is done for the K- without the Cholesky decomposition, which means that a random Gaussian vector with 0 mean and σ of the respective covariance matrix element is added to the ideal AliExternalTrackParam (fig. 23a). For each of the AliExternalTrackParam, the value of z is plotted against the dip angle $\tan \lambda$. Comparing the correlation coefficient $\sigma^{C}_{\tan \lambda} = -0.8278$ with the correlation value of the histogram $\sigma^{TH2F}_{\tan \lambda} = -0.82822$ (fig. 23b) one can see, that the multiplication of the random vector with the decomposed matrix correlates the parameters

according to the correlation coefficients given in the covariance matrix. Comparing the mean values and the RMS shows that the mean value is equal to the value of the respective element in the ideal ExternalTrackParam and the RMS is equal to the square root of the respective covariance matrix element.

6.7 Definition of the test cases

In order to test and verify the algorithmic implementation of the code, the following observables are implemented as test cases:

- reconstructed spatial position of the secondary vertex

- reconstructed transverse momentum of the mother

- reconstructed invariant mass of the mother

To quantify the precision of the reconstructed observables, the resolution is plotted against p_{T}, since all of the chosen observables have a p_{T} dependence. The resolution of an observable X is defined as the width of the distribution of the reconstructed values minus the Monte Carlo values, which is expected to be Gaussian:

$$Resolution = \sigma(X_{rec} - X_{MC}) \tag{65}$$

In figure 24a an example for a p_{T} integrated resolution of the position in x of a secondary vertex is shown. One can see, that it is an overlap of many Gaussian functions. This is due to the p_{T} dependence. Therefore all checks for the resolution are made in p_{T} bins. The mean value of the resolution has to be zero. To investigate, whether there is a bias, the mean value of the distribution of the MC values minus the reconstructed values is plotted against p_{T}. This is defined as the delta of the observable:

$$Delta = mean(X_{rec} - X_{MC}) \tag{66}$$

To have a check whether the errors of the observables are well estimated, the pull distribution is plotted. This is defined as the Gaussian width of the reconstructed value minus the Monte-Carlo value divided by the reconstructed error on that variable:

$$Pull = \sigma \left(\frac{X_{rec} - X_{MC}}{\sigma_X^{rec}} \right) \tag{67}$$

Since the difference between the reconstructed and the Monte Carlo values should be covered by the errors, the pull is expected to be a normal Gaussian distribution with zero mean and width equal to unity. An example for a pull distribution is shown in figure 24b. To investigate whether the estimation of the errors is biased, the width of the pull is plotted over p_{T}. The resolution, delta and pull are plotted for the different constraints of the KF: the mass constraint and the vertex constraint. To have a comparison with the vertexing tool recently used in ALICE, the secondary vertex is also reconstructed with the class AliVertexerTracks, which is typically used in the HF analysis. For the invariant mass, the common four vector addition serves as a comparison. Another important test is the χ^2/ndf distribution of the vertex fits, where ndf denotes the number of degrees of freedom. Its mean value is expected
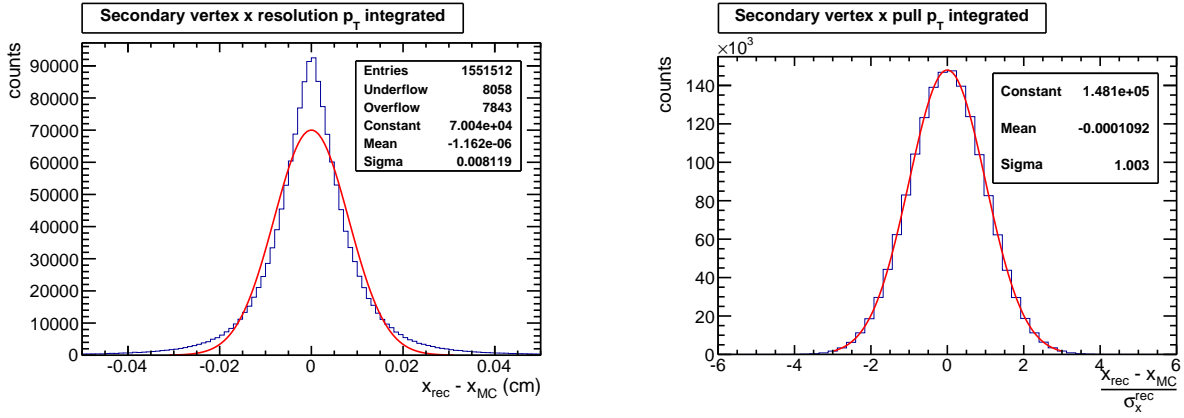
(a) Example for a resolution of the position in x of a secondary vertex.

(b) Example for a pull distribution of the position in x of a secondary vertex.

Figure 24

to be unity and is related to the sum of the pulls. The probability distribution of the χ^2 and the ndf has to be a flat distribution between zero and one. A mean value of the χ^2/ndf distribution that is higher than one indicates an underestimation of the errors of the fit and the probability is expected to increase towards zero, while a mean value of the χ^2/ndf distribution smaller than one indicates an overestimation of the errors and the probability distribution is expected to increase towards one.

45

7 Test Results of AliKFParticle

7.1 Quality of the daughters

In order to make statements about the performance of the vertexing software, it is crucial to check the quality of the daughter tracks. To verify the results of the fast simulation the same plots are made with the full Monte Carlo simulation on the sample LHC10f7a_d, which is a sample with added HF signals. This means that the production of heavy flavour in the collision is artificially enhanced. The sample LHC10f7a_d simulates proton-proton collisions and is one of the main sources for the HF analysis in ALICE. In general the full simulation provides a realistic simulation of the respective run of the real data. In the full simulation the whole detector material is taken into account. The traversing of the material by the particles is simulated with GEANT. For the analysis which uses the full simulation 6 ITS layers and at least 70 TPC clusters are required for the daughter tracks. Besides a TPC and ITS refit, a $\chi^2 < 4$ cut for the TPC clusters is applied. To obtain the resolution of the daughter tracks, the tracks are propagated to the DCA to the MC decay vertex of the mother particle. The comparison of the resolution of the track of the kaon as a function
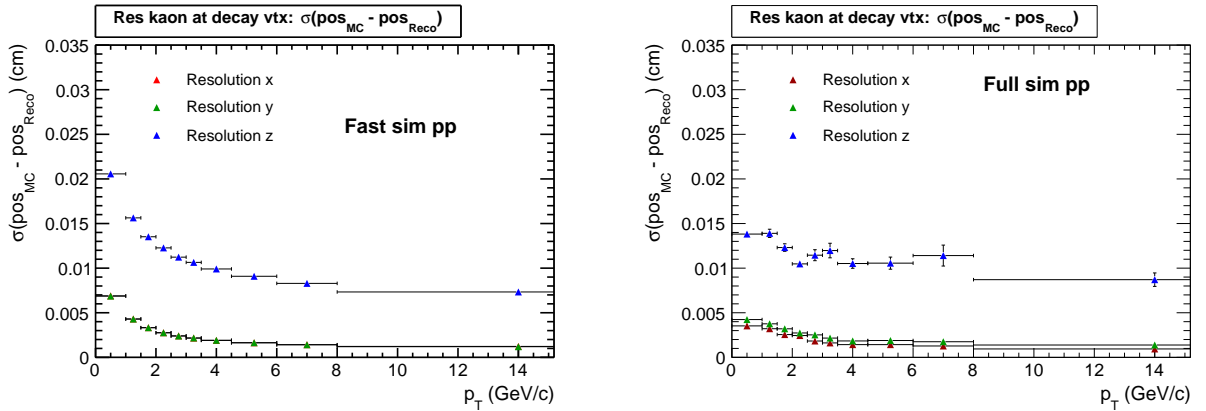
(a) Spatial resolution in x, y, z of the kaon track as a function of p_T in global coordinates at the decay vertex in the fast simulation. The red points are hidden under the green points.

(b) Spatial resolution in x,y,z of the kaon track as a function of its p_T in global coordinates at the decay vertex in the full simulation.

Figure 25

of its p_T in the fast simulation with the full simulation (fig. 25a and 25b) shows, that the resolution of the kaon in the fast simulation at the MC decay vertex is in good agreement with the full simulation, except in the first p_T bin. Here the resolution in the fast simulation is too low.

The resolution in z is worse than in x and y, which is not surprising, since the resolution of the detector in z is worse compared to the resolution in the transverse plane. The resolutions of x and y are expected to be the same. This can be observed in the fast simulation, while in the full simulation there is an asymmetry between x and y. The reason for this asymmetry is not understood yet and possibly only a feature of the sample LHC10f7a_d.

As required the pulls of the fast simulation (fig. 26a) are very close to unity. This is very important, since now the pulls of the reconstructed observables have to be also one
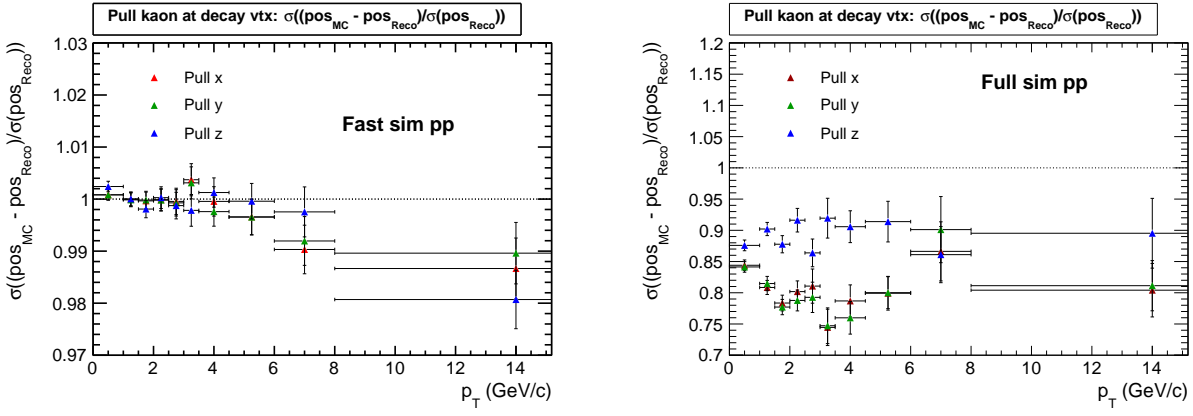
(a) Pulls of the kaon track as a function of its p_T at the MC decay vertex in x, y, z in the fast simulation.

(b) Pulls of the kaon track as a function of its p_T at the MC decay vertex in x, y, z in the full simulation.

Figure 26

and, if not, indicate that there is an issue with the implemented code. In the last p_T bin there is a deviation of about 2 %. Here higher statistics would be needed in order to check whether there is a small trend in the pulls of the fast simulation to overestimate the errors for increasing p_T. The pulls of the full simulation (fig. 26b) show, that the errors of the tracks are approximately overestimated by 20 % . Therefore the errors of the reconstructed values for the secondary vertex in the full simulation are expected to be also overestimated.

7.2 Reconstruction of the D^0

7.2.1 Secondary vertex

The secondary vertex is reconstructed from the two ESD tracks of the kaon and the pion. As described in chapter 6.7, the secondary vertex is reconstructed with the ALICE vertexing tool AliVertexerTracks. The exact functionality used in AliVertexerTracks is AliVertexerTracks::VertexForSelectedTracks. This functionality is used in the recent HF analysis to reconstruct secondary vertices. It is required that the reconstructed vertex has two contributors and is inside the beam pipe. These cuts are applied to have consistency with the cuts used in the HF analysis.

Figure 27a shows the resolution as a function of p_T of AliVertexerTracks and of AliKF with the two constraints in the fast simulation. AliKF gives a slightly better resolution than the AliVertexerTracks. The mass constraint gives only a very small improvement compared to the unconstrained AliKF. A strong improvement, especially in the low p_T range is obtained by constraining the reconstructed particle to the MC primary vertex. Comparing this plot to the plot of the full simulation (fig. 27b) shows that here the topological constraint is significantly worse and gives even worse results than the unconstrained fits for transverse momenta higher than ≈ 2.5 GeV/c. The reason for this is, that in the case of the full simulation the particle is constrained to the ESD primary vertex that has an uncertainty. This shows that the results of the resolution with the topological constraint depend strongly on the precision of the primary vertex. Therefore the topological constraint will be investigated in detail in
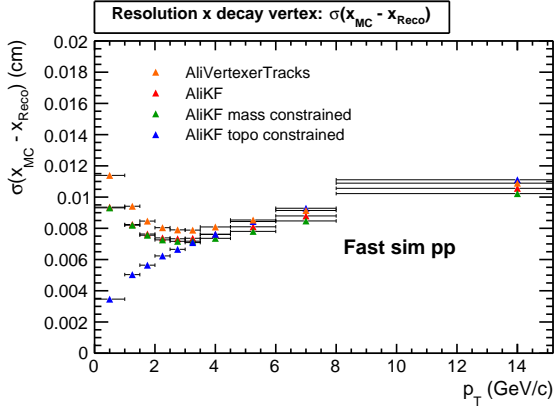
(a) Resolution in x of the position of the decay vertex of the D^0 as a function of its p_T in the fast simulation. For the topological constraint the MC primary vertex is used.
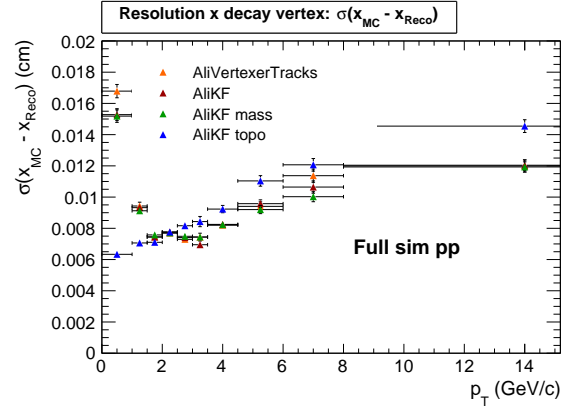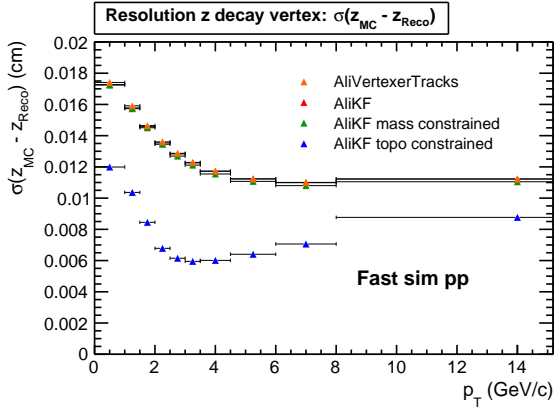
(b) Resolution in x of the position of the decay vertex of the D^0 as a function of its p_T in the full simulation. For the topological constraint the ESD primary vertex is used.
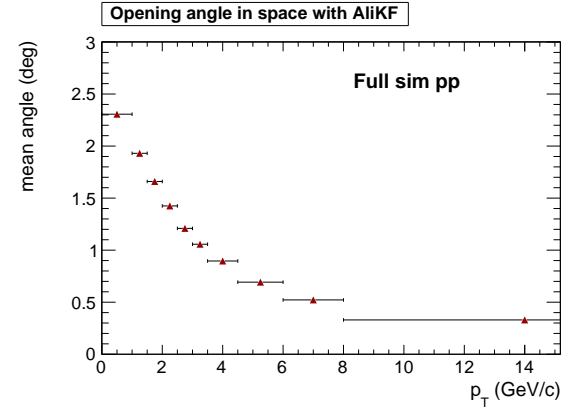
Figure 27

chapter 9.3.

Another important information is that all resolutions of the different vertex fits in the fast simulation show qualitatively the same behaviour as the fits in the fast simulations which confirms that the fast simulation gives reliable results. The statistics of the full simulation is limited, so that no quantitative statements about the difference in the vertexing performance between the AliVertexerTracks, unconstrained AliKF and mass constrained AliKF can be made.

(a) Resolution of the position in z of the decay vertex of the D^0 as a function of its p_T in the fast simulation.

(b) Opening angle between the kaon and the pion as a function of the p_T of the D^0 in the full simulation with AliKF.
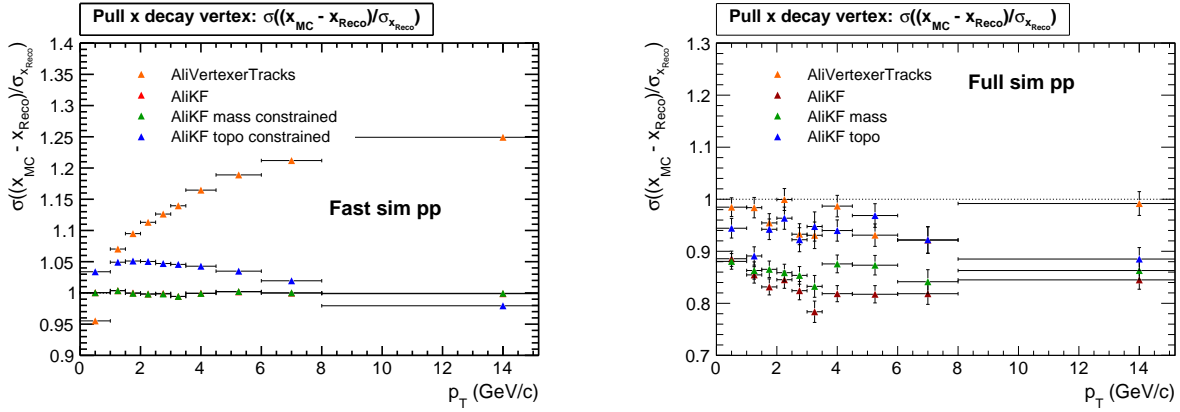
Figure 28

In z (fig. 28a) the resolution is slightly improved by the mass constraint compared to the AliVertexerTracks in the fast simulation. Also here a significant improvement is obtained by constraining the particle to the MC primary vertex. Although the resolution of the daughter tracks in z is factors worse than the resolution in x, the resolution of the secondary vertex

in z is never more than a factor 2 worse than the resolution in x.

The behaviour of the resolution of AliVertexerTracks, the unconstrained AliKF and the mass constrained AliKF is dominated by the resolution of the daughters and the opening angle between the daughters. The vertexing algorithms get more precise results when the opening angle between the daughters is larger. Therefore the resolution of the secondary vertex is worse in the low p_T region due to the worse resolution of the daughters and also gets worse in the high p_T region due to the decreasing opening angle. The opening angle obtained with AliKF in the full simulation is shown in figure 28b. The best resolution is obtained for a p_T between 3 GeV/c and 4 GeV/c, where both effects are moderate.

The pulls of the position of the secondary vertex reconstruction show that the errors

(a) Pull of the position of the decay vertex in x as a function of the p_T of the D^0 in the fast simulation.

(b) Pull of the position of the decay vertex in x as a function of the p_T of the D^0 in the full simulation.

Figure 29

of the AliKF are well estimated. In the fast simulation (fig. 29a) one can see that the pulls of the AliKF and the AliKF mass constrained are, as expected, close to unity, while the pull of the AliKF topological constraint differs by 5 %, which is still acceptable. The AliVertexerTracks shows a behaviour that is not understood yet. In the fast simulation it has a bias towards larger p_T. Since the pulls of the daughters in the full simulation were about 0.8, the pulls of the reconstructed vertex are expected to also be around this value. This is the case for the AliKF and also for the AliKF mass constrained (fig. 29b). The pull of the topological constraint shows qualitatively the same behaviour as in the fast simulation and is also too high. However, the AliVertexerTracks shows no bias in the full simulation and gives pulls that are very close to unity. The difference between the behaviour in the fast simulation and in the full simulation of this tool should be checked in the future, especially why AliVertexerTracks gives perfect pulls, although the daughter errors are overestimated. The mean values of the vertex position as a function of p_T (fig. 30a, 30b) show that there is no bias in the reconstruction of the vertex. The values are distributed randomly around the true MC positions for both the fast and the full simulation.
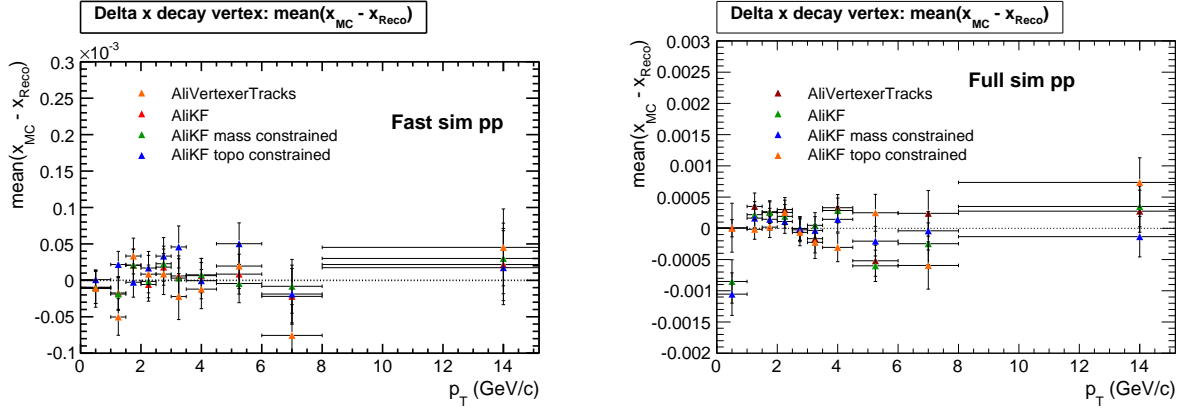
(a) Delta of the position of the decay vertex in x as a function of the p_T of the D^0 in the fast simulation.

(b) Delta of the position of the decay vertex in x as a function of the p_T of the D^0 in the fast simulation.

Figure 30

7.2.2 χ^2/ndf and probability

For the unconstrained AliKF vertex fit and for the two constrained vertex fits the distributions of the χ^2/ndf and the probability are investigated. As comparison also AliVertexerTracks is shown. For the fast simulation the χ^2/ndf distribution is expected to have a mean value of one, while for the full simulation the mean value of the χ^2/ndf distribution is expected to be approximately 0.8, since the errors of the daughters are 20 % overestimated which should reflect in the mean value of the χ^2/ndf distribution. The distribution of
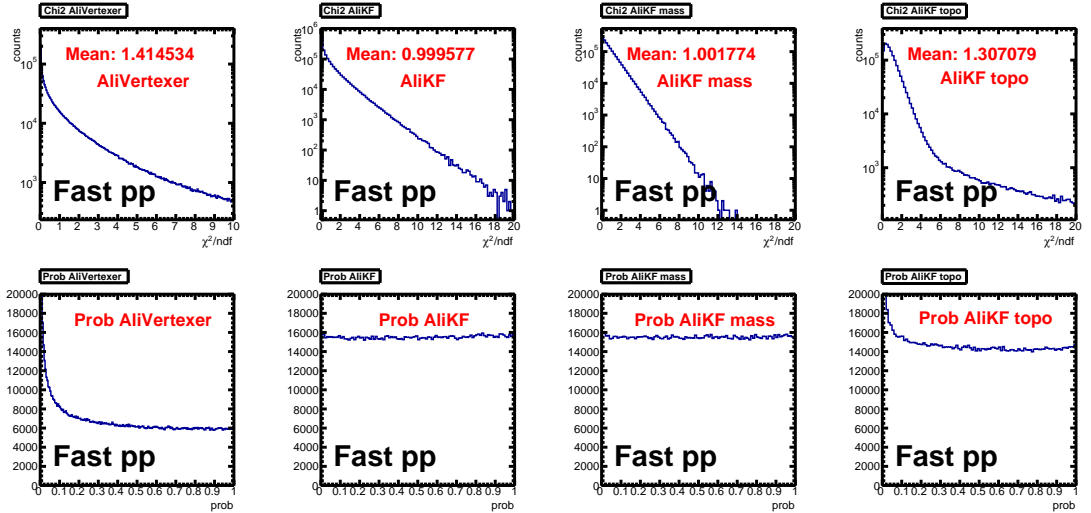
Figure 31: The top panel shows the χ^2/ndf distribution of the different vertexer in the fast simulation. The bottom panel shows the respective probability distribution.

the χ^2/ndf in the fast simulation is shown in figure 31 and confirms what has been seen in the pulls of the resolution. The AliVertexerTracks underestimates the error and thus has a mean value that is higher than one and the probability distribution increases in the first
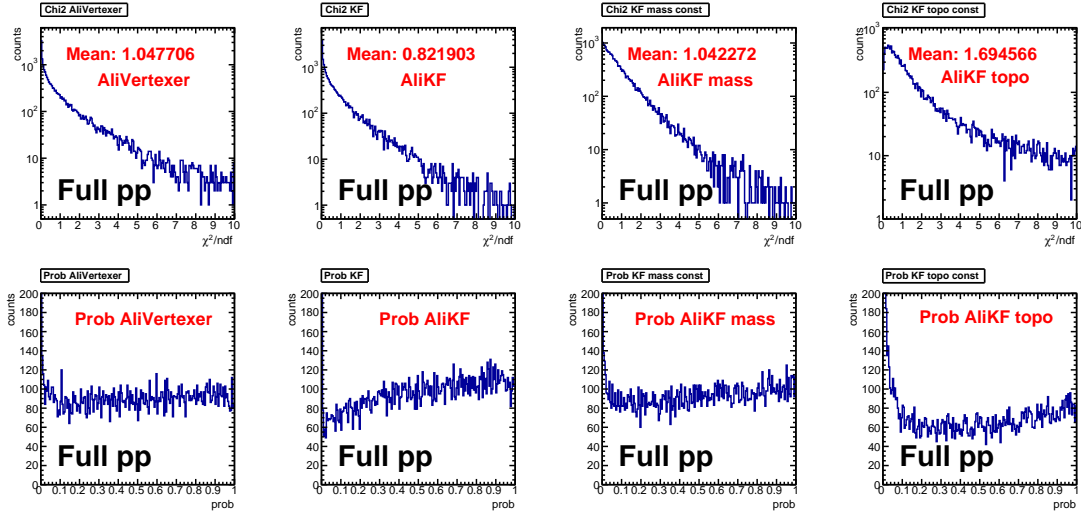
50

Figure 32: The top panel shows the χ^2/ndf distribution of the different vertexer in the full simulation. The bottom panel shows the respective probability distribution.

bins. The mean values of the χ^2/ndf distributions of the unconstrained AliKF and the mass constrained fit are close to unity and their probability distributions are flat. The mean value of the χ^2/ndf distribution of the topological constraint shows that here the uncertainty is underestimated, which also reflects in an increase of the probability distribution in the first bins. The mean values of the χ^2/ndf distributions of the vertexer in the full simulation are shown in figure 32 and also match with the observations made in the pulls of the resolution. AliVertexerTracks gives a perfect χ^2/ndf distribution, although the errors of the daughter tracks are overestimated. The unconstrained AliKF fit reflects the overestimation of the errors of the daughter in its χ^2/ndf distribution. This is also reflected by an increase of the probability distribution. The mean values of the χ^2/ndf distributions of the mass constraint and the topological constraint are both too high. Especially the χ^2/ndf distribution of the topological constraint has to be checked in the future.

7.2.3 Transverse momentum

The transverse momentum reconstruction is a feature that actually none of the used ALICE tools can provide. The AliKF is the only vertexing package in ALICE that constructs the whole mother particle. It is often convenient to plot the relative p_{T} resolution:

$$\frac{p_{\mathrm{T}}^{rec} - p_{\mathrm{T}}^{MC}}{p_{\mathrm{T}}^{rec}} \tag{68}$$

The resolution of the AliKF for the unconstrained and the two constrained reconstructions with the fast simulation are shown in figure 33a. The p_{T} resolution depends on p_{T} as described in section 5.3. In the variable $\frac{\sigma_{p_{\mathrm{T}}}}{p_{\mathrm{T}}}$ the multiple scattering effect is a constant for high momenta and the detector uncertainty increases linear with p_{T}, while for low momenta the multiple scattering effect becomes proportional to $\frac{1}{p_{\mathrm{T}}}$ because of the β dependence. This behaviour can be observed well for the unconstrained fit and the constrained fits. The mass constraint improves the momentum resolution significantly. The same effects can be seen in
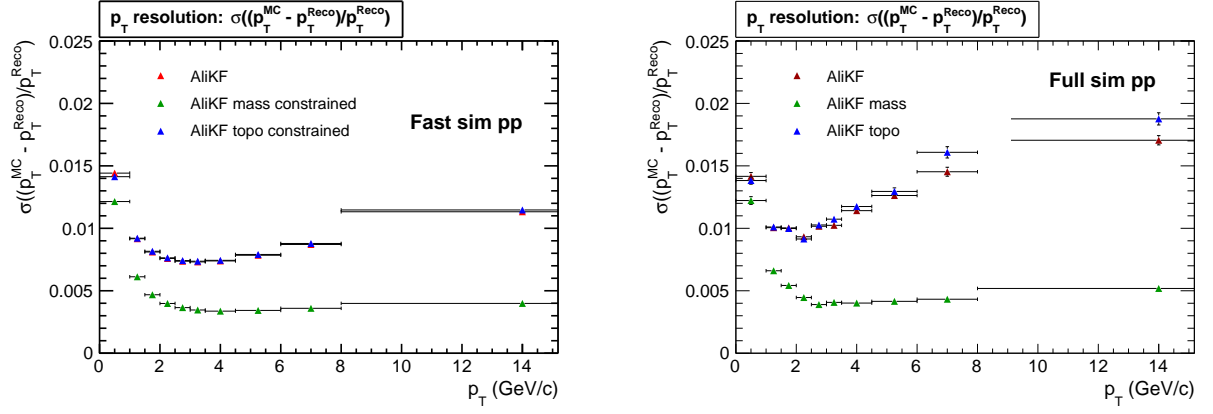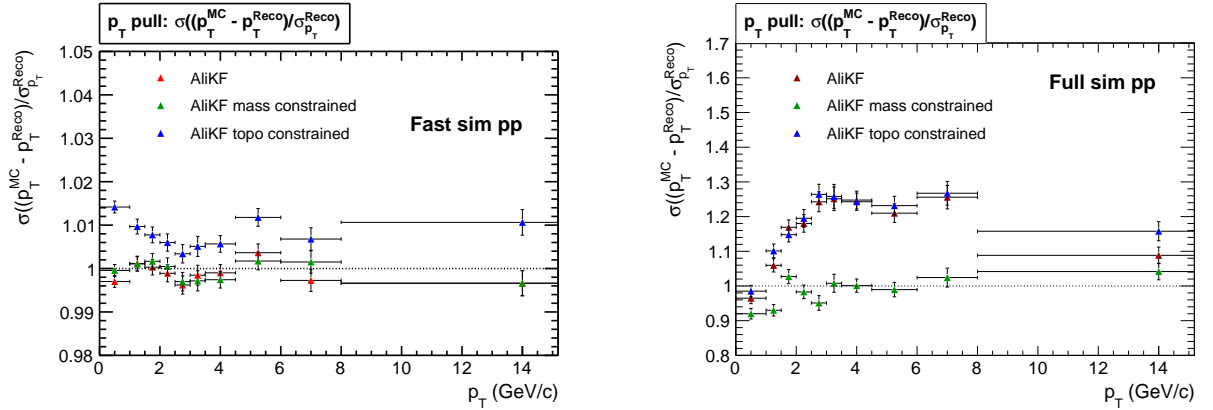
(a) Resolution of the transverse momentum of the D^0 in the fast simulation.

(b) Resolution of the transverse momentum of the D^0 in the full simulation.

Figure 33

the full simulation (fig. 33b). In the full simulation the topological constraint gives slightly worse results than the unconstrained fit.

In the high-p_T region, the resolution in the fast simulation is too high. This is not surprising, since in the parametrization of $\frac{q}{p_T}$ of the tracks (fig. 17b), the φ dependence is neglected and as shown in the residuals the uncertainty of the transverse momenta in the high-p_T region is underestimated. Although no energy correction is made, the description provided by the fast simulation is consistent with the full simulation in the low-p_T region.

The pulls in the case of the fast and the full simulation are shown in figure 34a and 34b. In

(a) Pulls of the transverse momentum of the D^0 in the fast simulation.

(b) Pulls of the transverse momentum of the D^0 in the full simulation.

Figure 34

the fast simulation, the pulls of the fits are close to unity, as it is required in case of a correct algorithmic implementation. The topological constraint deviates by about 5 percent, but the errors are well estimated. In the full simulation the pull for the mass constraint is close to unity. The pull in the case of the unconstrained fit has the same behaviour as the pull of the topological constraint. Both pulls show that the errors are overestimated by up to 30
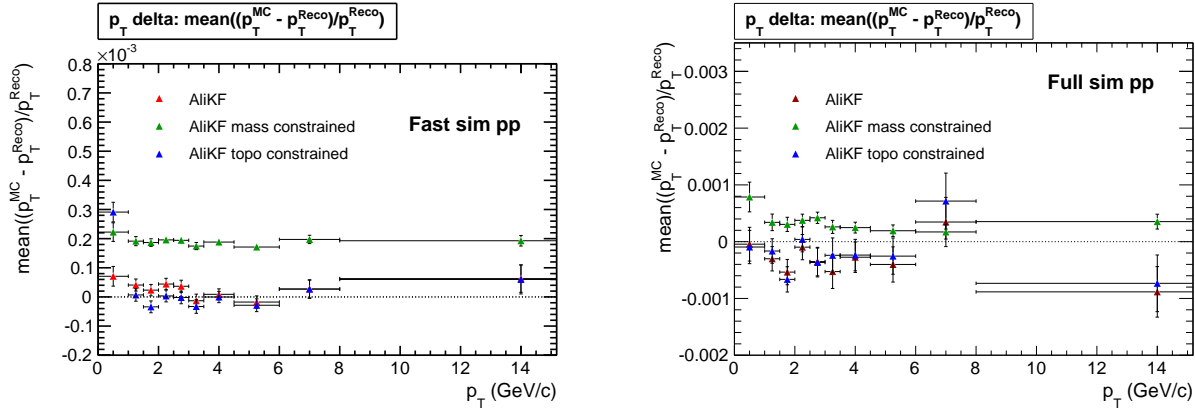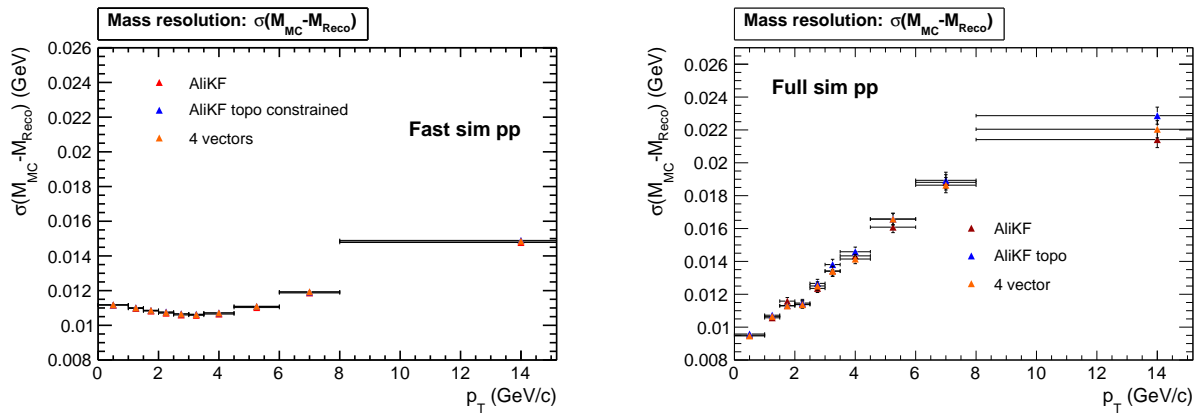
(a) Delta of the transverse momentum of the D^0 in the fast simulation.

(b) Delta of the transverse momentum of the D^0 in the full simulation.

Figure 35

percent. In figure 35a and 35b the delta of the p_T is plotted. It can be seen, that there is a small bias in the fit with the mass constraint, both for the fast and for the full simulation.

7.2.4 Invariant mass

(a) Resolution of the invariant mass of the D^0 as a function of its p_T in the fast simulation. The blue and red points are hidden under the orange points.

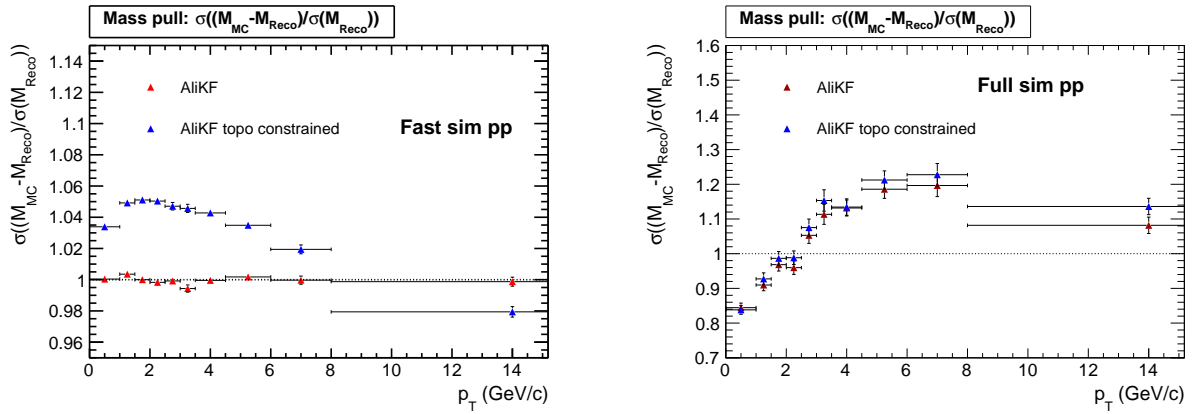(b) Resolution of the invariant mass of the D^0 as a function of its p_T in the full simulation.

Figure 36

For the invariant mass, the unconstrained fit, the topologically constrained fit and the calculation by four vectors is compared. Since the mass constraint assumes a certain mass of the mother particle, no meaningful resolution and error can be calculated. The four vectors calculation is done by estimating the energy of the daughter particles assuming their perfect MC mass and the momentum of the track:

$$E = \sqrt{M_{MC}^2 + \boldsymbol{p}_{track}^2} \tag{69}$$

53

The invariant mass of the mother is then obtained by adding the two four vectors of the daughters (p_x, p_y, p_z, E). The results of the resolution obtained with the different fits are shown in figure 36a and 36b. It can be seen that neither in the fast nor in the full simulation an improvement of the mass resolution can be seen using the AliKF. Moreover, it can be seen, that the description provided by the fast simulation is not in a good agreement with the full simulation. However, both in the fast and in the full simulation a deterioration of the resolution towards higher transversal momenta can be seen. Since the momentum plays a crucial role in the reconstruction of the invariant mass, it does not surprise that the resolution is too high in the fast simulation in the high-p_T region, as it was also seen for the p_T resolution.

The pulls of both the constrained and unconstrained fit of the fast simulation in figure 37a

(a) Pull of the invariant mass of the D^0 as a function of its p_T in the fast simulation. For the four vectors no pull is calculated.

(b) Pull of the invariant mass of the D^0 as a function of its p_T in the full simulation. For the four vectors no pull is calculated.
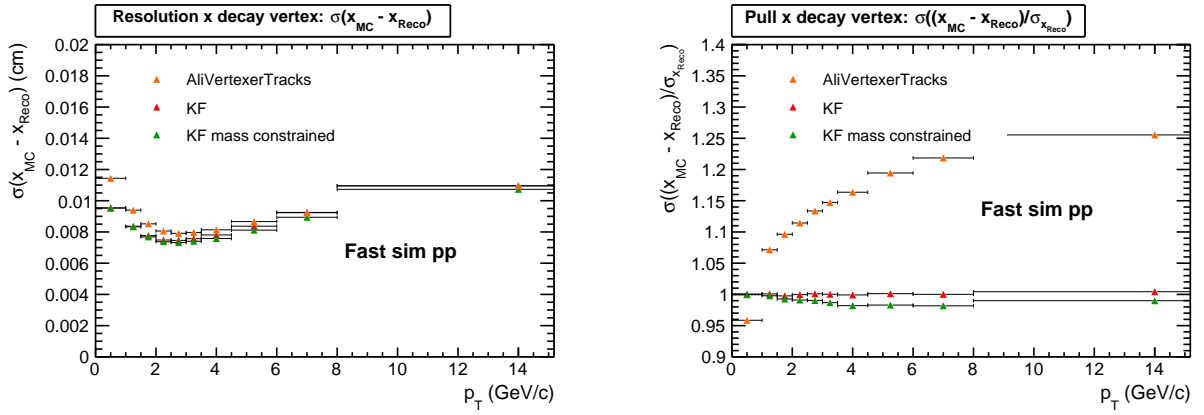
Figure 37
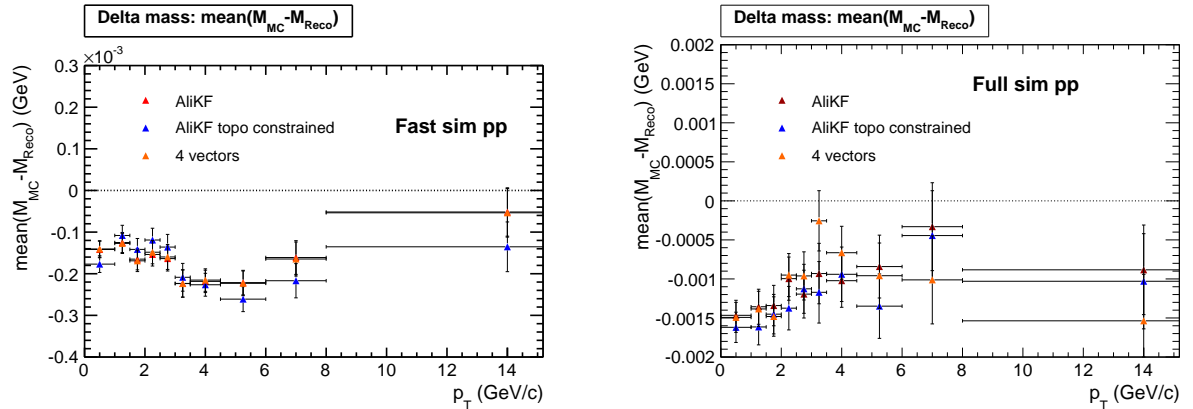
(a) Delta of the invariant mass of the D^0 as a function of its p_T in the fast simulation.

(b) Delta of the invariant mass of the D^0 as a function of its p_T in the full simulation.

Figure 38

are close to unity. As for the previous observables, the pull of the topological constraint

54

deviates by about 5 percent. The errors of the four vectors are not calculated, therefore no pull is shown. In the full simulation in figure 37b the pulls show the same behaviour as the pulls of the transverse momenta. Again the behaviour of the unconstrained fit is similar to the behaviour of the topological constraint. For the low momenta the errors are underestimated by up to 15 percent, while for high momenta the pulls are overestimated by up to 20 percent. In figure 38a and 38b the deltas are shown. Both in the fast and the full simulation the invariant mass is slightly biased. Since this is also observed for the four vector reconstruction, this seems not to be a problem of the AliKF, but seems to originate from the tracks themselves. However, the bias is small compared to the mass of the D^0 which is approximately $1,8696 \pm 0.0002$ GeV , while the bias is in the order of a few MeV for the full simulation.
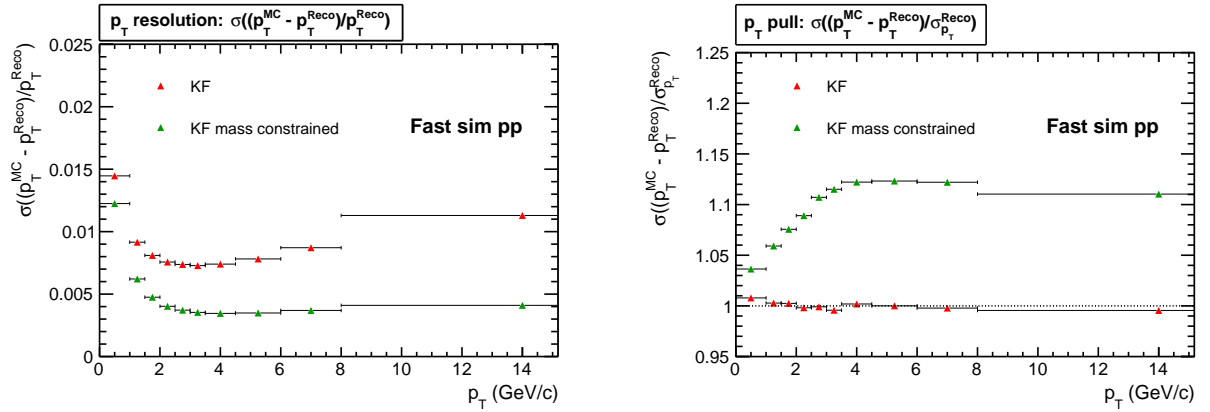
8 Test Results of KFParticle

(a) Resolution of the secondary vertex in x of the D^0 in the fast simulation with KFParticle.

(b) Pull the secondary vertex in x of the D^0 in the fast simulation with KFParticle.

Figure 39

The same tests which were shown for the AliKFParticle are made also for the new unified version of KFParticle. After the discovery of issues with the estimation of errors, the code has been modified by the developers. Since the topological constraint of the unified version is still under investigation, it is not shown. Moreover at the moment no AliROOT version which includes the unified KFParticle version is available. Thus no comparison to the full simulation can be made and only the fast simulation is investigated. However, the results in the previous section showed, that the fast simulation is in good agreement with the full simulation for the secondary vertex reconstruction and the transverse momentum. In figure 39a the resolution of the secondary vertex position in x calculated with the new KF version is shown.
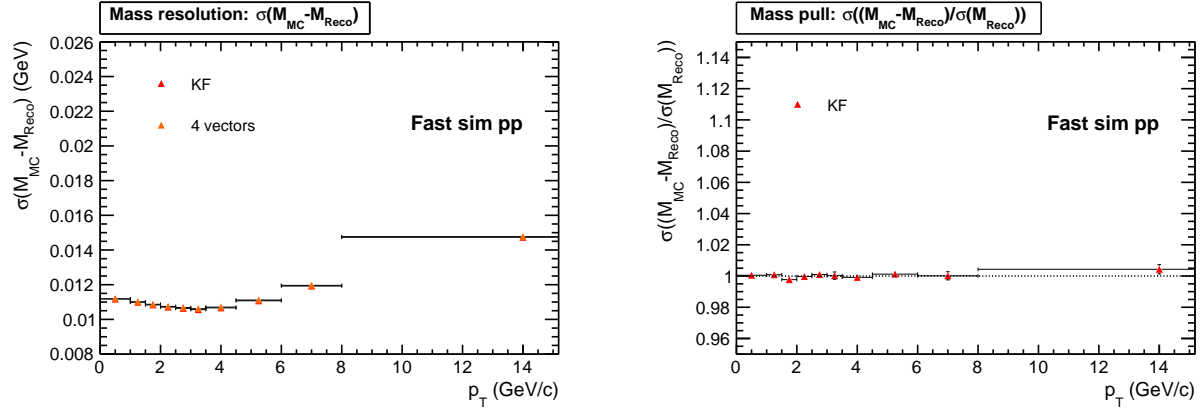

(a) Resolution of the transverse momentum of the D^0 in the fast simulation with KFParticle.

(b) Pull of the transverse momentum of the D^0 in the fast simulation with KFParticle.

Figure 40

Comparing this to the results obtained with AliKF shows, that the results are matching. In

the high-p_T region the KF is slightly worse than the AliKF. The pulls of the unconstrained and the mass constrained fit in figure 39b are close to unity. This shows that after the improvements of the code in the new unified version the errors are now well estimated.

The results of the p_T resolution are shown in figure 40a. For the transverse momentum resolution the results obtained with the KFParticle version are the same as the results with AliKFParticle. However, the pulls of the unified KFParticle version, shown in figure 40b, indicate that the errors calculated with KFParticle are underestimated, because the pull is significantly too large. This behaviour has to be investigated in the future. The resolution of the invariant mass is shown in figure 41a.

(a) Resolution of the invariant mass of the D^0 in the fast simulation with KFParticle.

(b) Pull of the invariant mass of the D^0 in the fast simulation with KFParticle.

Figure 41
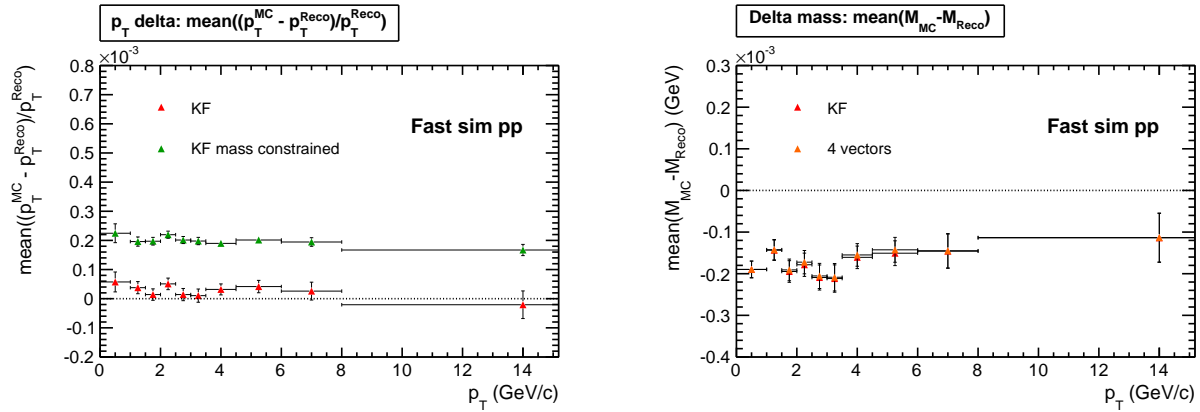
(a) Delta of the transverse momentum in the fast simulation with KFParticle.

(b) Delta of the invariant mass in the fast simulation with KFParticle.

Figure 42

Also the mass resolution calculated with KFParticle gives the same results as the fits with AliKFParticle.

The pull of the KF in figure 41b shows that the unconstrained fit estimates the errors on the invariant mass well. As it was observed for the AliKF, the mass constraint for the p_T is

57

slightly biased, as well as all calculations of the invariant mass as shown in figure 42.

The last important checks are the distributions of the $\chi^2/$ ndf and the probability of the vertex fit. This is shown in figure 43 for the unconstrained and the mass constrained fit. Both the distribution of the $\chi^2/$ ndf and the probability indicate that the fit is not optimal. The mean value of the $\chi^2/$ ndf distribution is higher than unity which also reflects in the probability. Compared to the distribution of the $\chi^2/$ ndf of the AliKF fit, this is a deterioration and has to be corrected in the future.
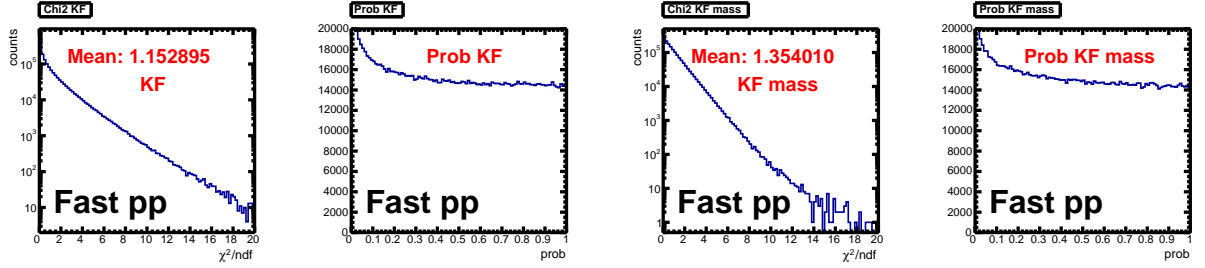

Figure 43: $\chi^2/$ ndf and probability of the unconstrained and the mass constrained fit with KFParticle.

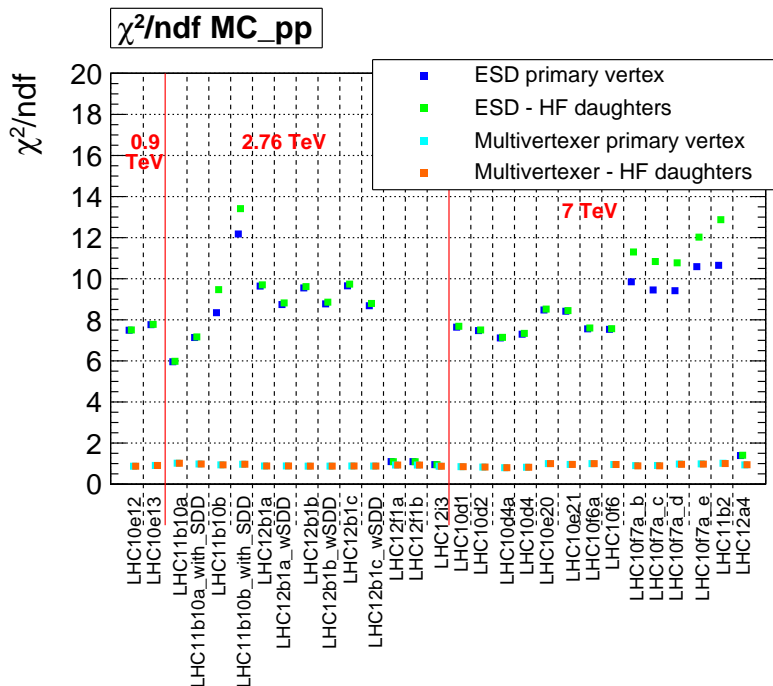# 9 Primary Vertex and Impact Parameter with AliKFParticle

Figure 44: Mean values of the χ^2/ndf for all available MC pp samples at GSI with and without refit with the Multivertexer.

The precision of the primary vertex plays a crucial role in the HF analysis. A great issue in this analysis is the inclusion of daughter tracks in the primary vertex, that come from HF decays and thus worsen the resolution of the primary vertex because they are not originating from it. The KF software provides powerful tools to correct the primary for these effects. Since the KF constructs the whole particle at the secondary vertex, it is possible to include the HF particle in the primary vertex fit. The results of these operations will be investigated in the following section.

9.1 Primary ESD vertex

During first tests of the quality of the primary it was seen, that the mean value of the χ^2/ndf distribution was systematically too high in the MC pp sample LHC10f7a_d. Therefore all available MC samples and samples of real data at GSI have been checked for the spatial resolution, pulls and the mean values of the χ^2/ndf distribution. This is shown in figure 44. Additionally it was checked how these values change when all HF daughters are removed via the function AliVertexerTracks::RemoveTracksFromVertex. It is expected, that the χ^2/ndf distribution improves after the removing of the daughters, since the fit is closer to the truth then. However, it was seen, that the removal of the HF daughters gave no significant improvement of the χ^2/ndf distribution. Further investigations showed that many samples had the same problem. For Monte Carlo samples produced after a certain date in 2012 the mean

values of the χ^2/ndf distributions are close to unity again. The reason for this is the implementation of a new vertexing package, called the Multivertexer. It is possible to refit older samples with this tool. As shown in the figure, this solves the problems and gives meaningful χ^2/ndf distributions with mean of around unity again. Therefore it is recommended to refit ESDEvents of older samples with: AliESDUtils::RefitESDtracks(ESDEvent,6).

9.2 Improvement of the resolution

For the MC sample LHC10f7a_d it is investigated how the resolution of the primary vertex changes by recalculating it with different functionalities. After the preliminary considerations in the previous section, the original ESD primary vertex is refitted with the Multivertexer. For every D^0 that comes from the primary vertex it is probable that there is a second charmed hadron coming from the creation of the charm anti-charm pair in the collision. Therefore as a first check all included heavy flavour daughters are removed from the primary vertex . The second tested case is the removal of the daughters of only one side of this charm anti-charm pair which is closer to realistic analysis situations. This means that for every found D^0 the pion and kaon are removed. This is done with the ALICE tool AliVertexerTracks::RemoveTrackFromVertex and with the functionalities that AliKF provides to recalculate the primary. In the last tested case the daughters of the D^0 are removed and the D^0 reconstructed with the AliKF is added to the primary vertex fit. The results are
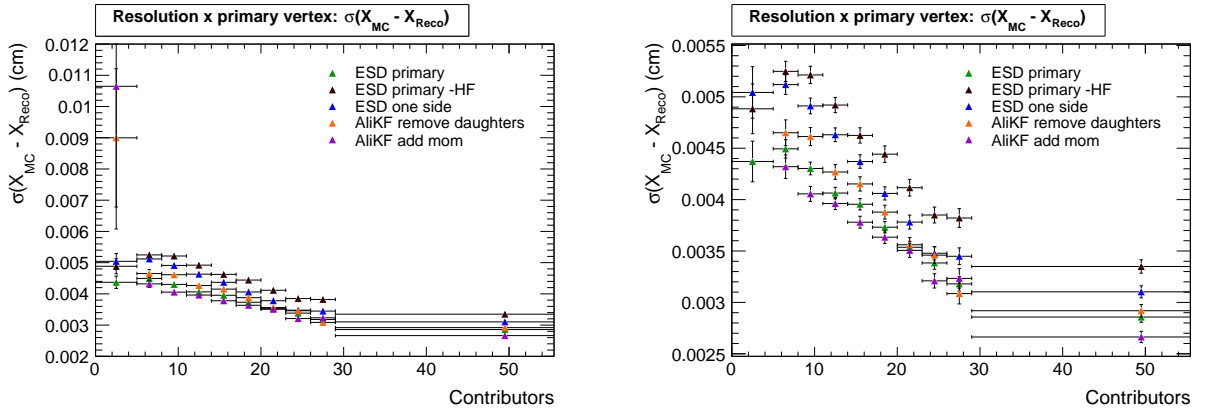
(a) Resolution of the primary vertex with AliKF in x in the full simulation after various recalculations.

(b) 45a in a different scale.

Figure 45

presented in figure 45a and 45b. As can be seen, the resolution of the primary vertex is depending on the contributors. Therefore, by removing the daughters only, the resolution worsens, although the removed tracks are not originating from the primary vertex. This effect is strongest, when all HF daughters are excluded. By removing only one side of the charmed quark pair, the resolution is still worse, but it can be seen, that the AliKF provides better results than the ALICE tool. By adding the mother after the removal of the daughters an improvement of the resolution is obtained although one contributor is lost. The delta of the primary vertices shows, that there is a bias in the primary vertex obtained with AliKF

after the removal of the daughters (fig. 46a). However, after the addition of the mother no bias is seen any more.

Another interesting feature of the primary vertices can be seen in the point with the lowest number of contributors. Here the ESD vertices provide significantly better results. This is due to the influence of the diamond constraint that gives additional information and thus is very useful in the low contributors region. The improvement of the resolution by removing the daughters and adding the mother has some important consequences for the resolution of observables that are depending on the precision of the primary vertex. This will be investigated in the following sections.

9.3 The topological constraint

As already described in section 7.2.1 the topological constraint depends strongly on the primary vertex precision. Thus the topological constraint is applied and tested again after the removal of the daughters and the addition of the mother. The spatial resolution is plotted again. For comparison the constraint to the ideal MC primary is also plotted. The
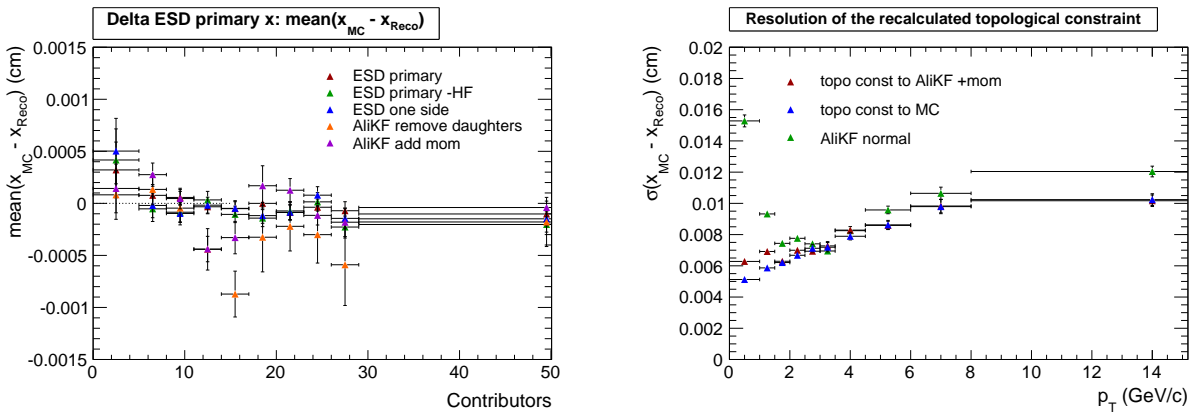
(a) Delta of the different primary vertices.

(b) Topological constraint to different primary vertices.

Figure 46

results are shown in figure 46b. It can be seen that the topological constraint to the MC primary shows qualitatively the same behaviour as the constraint to the MC vertex in the fast simulation in figure 27a. Comparing this to the result of the ESD primary vertex in the full simulation obtained in this section, a significant improvement of the resolution can be seen. In the high-p_T region the resolution is close to the ideal resolution obtained with the constraint to the MC primary vertex. In the low-p_T region the resolution is still better than the one of the unconstrained AliKF fit. Therefore it is mandatory to first remove daughters and add the mother if the topological constraint is used.

9.4 Impact parameter

Another observable that provides very useful information for the HF analysis is the impact parameter of the daughter tracks to the primary vertex. This is equal to the DCA of the

daughters to the primary vertex and needs to be measured with very high precision. To calculate the resolution of the impact parameter, ideal ESD tracks are created from the MC daughters. The DCA between the MC primary vertex and the ideal MC daughter track is calculated, which gives the true MC impact parameter. The measured impact parameter reflects the uncertainty on the primary vertex and of the track. In figure 47 the results of
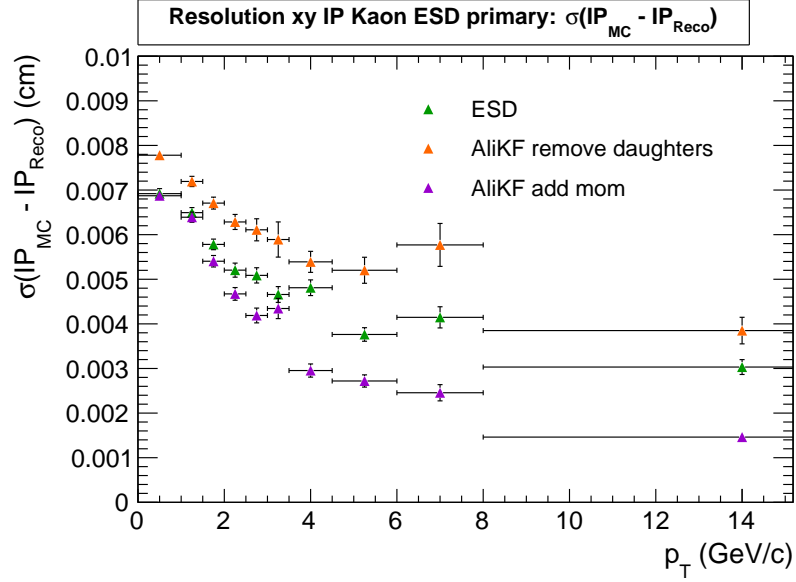

Figure 47: Impact parameter in the xy plane to different primary vertices as a function of the track transverse momentum.

the impact parameter of the Kaon to the original ESD primary vertex, the AliKF vertex with removed daughters of one side of the charm quark pair and the AliKF vertex with the removed daughter and added D^0 is presented. The plot shows that the resolution of the impact parameter depends very strongly on the resolution of the primary vertex. As expected, the resolution worsens with the removal of daughters, but improves significantly after the addition of the mother. In the low-p_T region no improvement is seen. One possible hypothesis for this is, that in this region the resolution is dominated by the track error.

10 Conclusion and Outlook

10.1 Test of AliKF

The tests have shown, that for the decay of the D^0 the parameters are well estimated by the AliKF. The resolution of the position of the secondary vertex can be improved by applying the topological constraint after the removal of the daughter tracks and the addition of the mother to the primary vertex fit. The resolution of the transverse momentum can be improved by the application of the mass constraint. The mean value of the χ^2/ndf distribution of the topological constraint is significantly higher than unity, while the unconstrained fit provides excellent results. An improvement in the resolution of the impact parameter can be obtained by improving the resolution of the primary vertex. Since the development of AliKF will not be continued, the results of this test now serve as a benchmark for the debugging of the new version.

10.2 Test of KF

After the debugging of the code by the authors, the new version of KFParticle now gives pulls that are close to unity for the D^0 decay in the fast simulation, except for the transverse momentum where the pull of the mass constraint is biased. The results for the resolutions are mostly the same as the ones obtained with AliKF. The mean values of the χ^2/ndf distributions of the unconstrained fit and the constrained fit have to be checked again. The tests that are made for the topological constraint for AliKF have to be done for the KF as soon as the debugging of the topological constraint is finished. Since KF will be the version of the future it is mandatory to at least reach the same performance that AliKF can provide at the moment.

10.3 Further checks on the vertexer

In the future some more checks for the AliVertexerTracks, AliKF and KF are necessary. The first important check is, whether there are numerical problems when switching from the 5x5 covariance matrix of the ALICE track model to the 6x6 covariance matrix of the KF model. Since in the latter representation one row of the covariance matrix is fully correlated, it is possible that eigenvalues of the covariance matrix get negative. This problem is also relevant for the switch from the local to the global system in ALICE. Another important test is, to reconstruct K_s^0 and Λ^0 decays, since they decay much later and thus the vertexers are confronted with new challenges. Moreover, the secondary vertex reconstruction with AliVertexerTracks has to be investigated.

10.4 The Unit Test

The unit test is a powerful tool to verify the algorithmic implementation of the vertexing code. The main purpose of the unit test - to have control over the input - is achieved already with the simple parametrization. Small deviations from the predicted output in the ideal case can be detected, as can be seen in the example of the mean value of the χ^2/ndf distribution of the KFParticle. It is planned to include a version of this test in AliROOT,

so that every new version of KF can be tested with the ideal input. Moreover, by making corrections for the various dependencies in the parametrization for the fast simulation, it is possible to develop a performance test that also takes into account the special features of the ALICE detector. Another important step would be to include a step between the ideal case and the test with the full simulation by making the pulls of the ideal case not Gaussian any more, so it can be seen on which stage the behaviour of the pulls in the full simulation deviates from the behaviour in the ideal case.
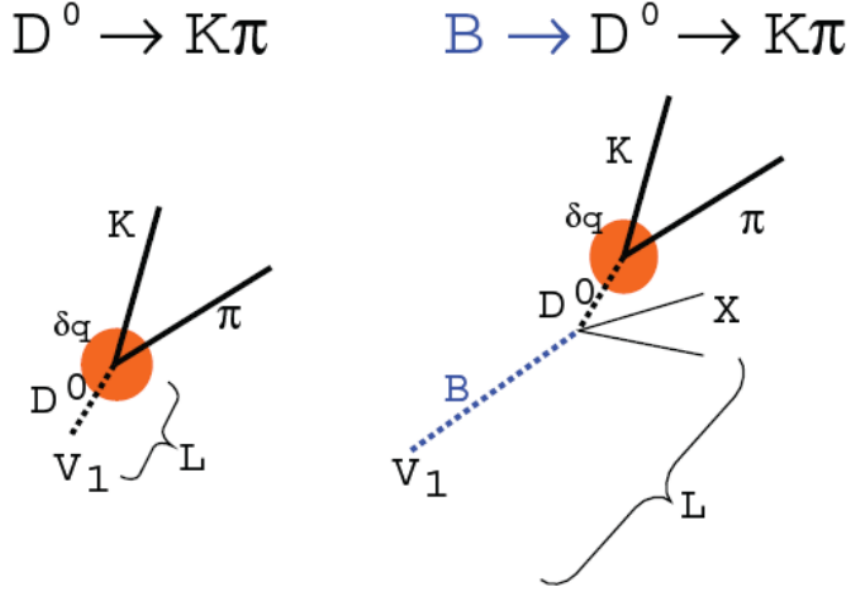
10.5 Planned physics analysis with KF

Figure 48: Sketch of a prompt and a feeddown D^0 [27].

In figure 48 a sketch of a prompt D^0 coming directly from the primary vertex and a feeddown D^0 coming from a B decay is shown. The ratio of the prompt and feeddown D^0, that is important for the determination of the charm cross section, has a large uncertainty. Since no existing methods can provide a precise measurement, this ratio is calculated from theory. Therefore the goal is to develop a reliable experimental method to measure this ratio. There are two crucial properties of feeddowns that are illustrated in the sketch and can be exploited for the analysis. First the B meson flies approximately 500 microns and the D^0 approximately 150 microns. Second the prompt D^0 points back directly to the primary vertex, while the feeddown D^0 that is produced in the decay of the B meson does not point directly to the primary. Therefore the D^0 will be constructed with the mass and the topological constraint from the pion and kaon daughters. The idea is that the χ^2/ndf of the vertex fit and the pseudo proper decay length of the D^0 give information whether the D^0 originates from the primary or not, because the χ^2/ndf should be deviating significantly from unity if the particle does not point back to the primary and the pseudo proper decay length should be too large. Thus it will be investigated whether it is possible to separate prompt and feeddown D^0 on a single candidate base.

References

[1]   R. Averbeck. "Heavy-flavor production in heavy-ion collisions and implications for the properties of hot QCD matter". In: *Prog.Part.Nucl.Phys.* 70 (2013), pp. 159–209. DOI: `10.1016/j.ppnp.2013.01.001`.

[2]   Christoph Berger. *Elementarteilchenphysik*. Springer, 2014.

[3]   (ed.) Sarkar S., (ed.) Satz H., and (ed.) Sinha B. "The physics of the quark-gluon plasma". In: *Lect.Notes Phys.* 785 (2010), pp. 1–369. DOI: `10.1007/978-3-642-02286-9`.

[4]   J. Schukraft. "Heavy Ion physics with the ALICE experiment at the CERN LHC". ALICE Collaboration. In: *Phil.Trans.Roy.Soc.Lond.* A370 (2012), pp. 917–932. DOI: `10.1098/rsta.2011.0469`. arXiv: `1109.4291 [hep-ex]`.

[5]   P. Braun-Munzinger and J. Stachel. "The quest for the quark-gluon plasma". In: *Nature* 448 (2007), pp. 302–309. DOI: `10.1038/nature06080`.

[6]   Betty Bezverkhny Abelev et al. "Performance of the ALICE experiment at the CERN LHC". ALICE Collaboration. In: *International Journal of Modern Physics A* 29.24 (2014), p. 1430044. DOI: `10.1142/S0217751X14300440`.

[7]   K. Aamodt et al. "The ALICE experiment at the CERN LHC". ALICE Collaboration. In: *JINST* 3 (2008), S08002. DOI: `10.1088/1748-0221/3/08/S08002`.

[8]   F. Carminati et al. "ALICE: physics performance report, volume I". ALICE Collaboration. In: *Journal of Physics G: Nuclear and Particle Physics* 30.11 (2004), p. 1517.

[9]   B. Abelev et al. "Measurement of charm production at central rapidity in proton-proton collisions at $\sqrt{s} = 2.76$ TeV". ALICE Collaboration. In: *Journal of High Energy Physics* 2012.7, 191 (2012). DOI: `10.1007/JHEP07(2012)191`. URL: `http://dx.doi.org/10.1007/JHEP07%282012%29191`.

[10] B. Abelev et al. "Measurement of electrons from beauty hadron decays in pp collisions at". ALICE Collaboration. In: *Physics Letters B* 721.13 (2013), pp. 13 –23. ISSN: 0370-2693. DOI: `http://dx.doi.org/10.1016/j.physletb.2013.01.069`. URL: `http://www.sciencedirect.com/science/article/pii/S0370269313001275`.

[11] Martin Völkl. "Measurement of beauty-hadron decay electrons in Pb–Pb collisions at $\sqrt{s_{NN}} = 2.76$ TeV with ALICE". ALICE Collaboration. In: (2014). arXiv: `1412.2670 [nucl-ex]`.

[12] MinJung Kweon. "Recent results on open heavy-flavour observables in relativistic nuclear collisions". ALICE Collaboration. In: *Nucl.Phys.* A931 (2014), pp. 155–164. DOI: `10.1016/j.nuclphysa.2014.08.080`.

[13] Sergey Gorbunov [Frankfurt University]. "On-line reconstruction algorithms for the CBM and ALICE experiments ". `https://www-alt.gsi.de/documents/DOC-2013-Dec-21.html`. PhD thesis. Mar. 2013.

[14] I. Kisel, I. Kulakov, and M. Zyzak. "Standalone First Level Event Selection Package for the CBM Experiment". CBM. In: *Nuclear Science, IEEE Transactions on* 60.5 (2013), pp. 3703–3708. ISSN: 0018-9499. DOI: `10.1109/TNS.2013.2265276`.

[15] S. Gorbunov and I. Kisel. "Reconstruction of decayed particles based on the Kalman filter". CBM. In: (2007). CBM-SOFT-note-2007-003.

[16] R. Frühwirth et al. *Data Analysis Techniques For High Energy Physics*. Cambridge University Press, 2000.

[17] B. Alessandro et al. "ALICE: Physics performance report, volume II". ALICE Collaboration. In: *Journal of Physics G: Nuclear and Particle Physics* 32 (2006), pp. 1295–2040.

[18] P. Billoir. "ERROR PROPAGATION IN THE HELIX TRACK MODEL". In: (1986). CERN-DELPHI 87-4, PROG 63.

[19] C. Grupen and B. Shwartz. *Particle Detectors*. Cambridge University Press, 2008.

[20] Yu Belikov, K. Safark, and B. Batyunya. "Kalman Filtering Application for Track Recognition and Reconstruction in ALICE Tracking System". ALICE Collaboration. In: (1997). ALICE-INT-1997-24, CERN-ALICE-INT-1997-24.

[21] A. Dainese and N. Carrer. "A parametrization of the Kalman Filter track reconstruction in the ALICE TPC". ALICE Collaboration. In: (2003). ALICE-INT-2003-011.

[22] Sigmund Brandt. *Data Analysis*. Springer, 1999.

[23] R.L. Glückstern. "Uncertainties in track momentum and direction, due to multiple scattering and measurement errors". In: *Nuclear Instruments and Methods* 24.0 (1963), pp. 381 –389. ISSN: 0029-554X. DOI: http://dx.doi.org/10.1016/0029-554X(63)90347-1. URL: http://www.sciencedirect.com/science/article/pii/0029554X63903471.

[24] M. Valentan, M. Regler, and R. Frühwirth. "Generalization of the Glückstern formulas II: Multiple scattering and non-zero dip angles". In: *Nuclear Instruments and Methods in Physics Research Section A: Accelerators, Spectrometers, Detectors and Associated Equipment* 606.3 (2009), pp. 728 –742. ISSN: 0168-9002. DOI: http://dx.doi.org/10.1016/j.nima.2009.05.024. URL: http://www.sciencedirect.com/science/article/pii/S0168900209009474.

[25] T. Sjöstrand, S. Mrenna, and P. Z. Skands. "PYTHIA 6.4 Physics and Manual". In: *JHEP* 0605 (2006), p. 026. DOI: 10.1088/1126-6708/2006/05/026. arXiv: hep-ph/0603175 [hep-ph].

[26] Mathworks. *Matlab, Random Number Generation*. URL: http://de.mathworks.com/help/matlab/ref/randn.html;jsessionid=7e33e0d62cdb52b50443592cf946.

[27] Francesco Prino. *Private Communication*. 2015.

*Acknowledgements

First and foremost, I would like to thank Silvia Masciocchi for the excellent supervision and the great encouragement during the last seven months. Then I would like to thank Marian Ivanov for the provision of many, many ideas and the support in the development of the code. Moreover, I am grateful to Johannes Stiller and Michael Winn for the help and for proofreading my thesis and to Klaus Reygers for reading and evaluating it. Furthermore I would like to thank Maksym Zyzak for the well working collaboration and Ruben Shahoyan for the patient and precise explanations. Special thanks go to my family and friends for the support during the last months.

*Erklärung

Ich versichere, dass ich diese Arbeit selbstständig verfasst und keine anderen als die angegebenen Quellen und Hilfsmittel benutzt habe.

Heidelberg, den 17.03.2015,

Lukas Layer